

**NUMERICAL INVESTIGATION OF ATMOSPHERIC ICING ON WIND TURBINE BLADES**

by © Galal Mohamed Galal Ibrahim

A thesis submitted to the School of Graduate Studies in partial fulfillment of the

requirements for the degree of

**Master in Mechanical Engineering**

Memorial University of Newfoundland

St. John's Newfoundland and Labrador

**March 2017**

## **Abstract**

The research work presented in this thesis aims to predict ice accretion effect on a wind turbine blade section at 80% of blade span. All simulations are obtained using FENSAP ICE, a widely used solver for aircraft in-flight icing simulations. Using low and high liquid water concentrations existed in clouds at lower altitudes, different icing events are simulated. Ice accretion predictions are computed using single-shot and multi-shot approaches. Blade surface roughness is investigated, as well as the relationships between ice mass, liquid water content, median volume diameter and temperature are predicted. To study the effect of blade design / curvature parameters on the ice formation process, ice accretion loads are predicted for all NREL airfoil families used for horizontal axis wind turbines. The effect of low and high LWC conditions on blade thickness is presented. Effects of atmospheric temperature, LWC, MVD and flow angle of attack on resulted ice shape are investigated. The degradation in aerodynamic characteristics due to ice formation is investigated at different icing conditions. The new numerical data presented in this thesis provide useful insights on ice accretion rates for wind turbines operating in cold and harsh environments.

## **Acknowledgments**

First and foremost, I praise God, my strength and my guide, for providing me this opportunity and granting me the capability to proceed successfully. I am also grateful for the numerous people who have assisted me in completing this degree.

I would like to thank my supervisors, Dr. Kevin Pope and Yuri Muzychka for their vision, guidance and support. Through their abundant patience, I have gained an immense amount of invaluable knowledge and experience.

I sincerely thank all my family who have supported me in reaching this milestone. Without their encouragement, I would have never pursued or completed this graduate degree. I can't express enough my gratitude and appreciation for their never ending support, love and always pushing me to go one step further.

## Table of Contents

Abstract.....	ii
Acknowledgments.....	iii
List of Figures .....	vi
Nomenclature .....	viii
Chapter 1 Introduction .....	1
1.1. Background.....	1
1.2. Research Objectives .....	1
1.3. Thesis Organization .....	2
Chapter 2 Literature review .....	3
2.1. Wind Power in Cold Regions .....	3
2.2. Icing Effects on Wind Turbines.....	4
2.3. Ice Growth on Wind Turbines .....	5
2.4. Ice Accretion Variables.....	6
2.5. Ice Accretion Mechanisms on Wind Turbines.....	7
2.6. Ice Accretion mitigation strategies on Wind Turbines.....	9
2.7. Ice Accretion Investigation on Wind Turbines .....	10
Chapter 3 Methodology .....	14
3.1. Mesh Discretization Scheme .....	14
3.2. Formulation of Multiphase and Phase Change .....	17
3.3. Single and Multi-Shot Approaches.....	21
Chapter 4 Results and Discussions.....	23
4.1. Ice Accretion Loads Using Single-Shot Approach.....	25

4.2. Roughness Effect on Ice Accretion.....	28
4.3. Ice Accretion Loads Using Multi-Shot Approach.....	30
4.4. Ice Load Predications on NREL Airfoil Families .....	33
4.5. Blade Thickness Effect.....	37
4.6. Effect of Flow Angle of Attack on Ice Shape .....	40
4.7. Icing Effect on Aerodynamic Performance .....	49
4.8. Results Validation.....	56
Chapter 5 Conclusions and Recommend Research .....	59
References .....	61

## List of Figures

Figure (1) Canada installed wind capacity over last 16 years taken from CANWEA, 2017 .4	
Figure (2) Ice growth configurations on a pitch controlled wind turbines (a) power generation, (b) idling, and (c) standstill modified from Battisti et. al. 2015 .....	5
Figure (3) Empirical relationship between ice type, wind speed and temperature by Fikke et. al. 2006 .....	8
Figure (4) NREL S809 airfoil profile .....	15
Figure (5) Grid discretizations for (a) elevation view of O grid and (b) cell distribution around the blade.....	16
Figure (6) Solution scheme for single-shot approach.....	21
Figure (7) Solution scheme for multi-shot approach.....	22
Figure (8) Variation of LWC with MVD in (a) stratiform clouds and (b) cumuliform clouds. ....	25
Figure (9) Ice accretion at several temperatures in (a) low LWC conditions (stratiform clouds) and (b) high LWC conditions (cumuliform clouds).....	26
Figure (10) Ice mass variation with time in (a) low LWC conditions (stratiform clouds) and (b) high LWC conditions (cumuliform clouds) .....	28
Figure (11) Ice accretion at different temperatures with applied surface roughness for (a) low LWC conditions (stratiform clouds) and (b) high LWC conditions (cumuliform clouds) .....	30
Figure (12) Ice mass variation with number of shots at -4°C in (a) low LWC conditions (stratiform clouds) and (b) high LWC conditions (cumuliform clouds) .....	32
Figure (13) Ice mass variation with number of shots at -4°C with applied surface roughness in (a) low LWC conditions (stratiform clouds) and (b) high LWC conditions (cumuliform clouds).....	33
Figure (14) Airfoil curvature characterizations .....	34
Figure (15) Ice mass variations with (a) blade maximum thickness and (b) $T_{Max} / X_{Mean}$ ..	36
Figure (16) Ice loads on NREL airfoil families for HAWTs .....	37

Figure (17) Ice mass variation with blade thickness for (a) low LWC conditions and (b) high LWC conditions .....	40
Figure (18) Power coefficient distribution variation for (a) chord length projection on the X-axis and (b) blade height projection on the Y-axis .....	41
Figure (19) Droplet LWC concentrations variation for (a) chord length projection on the X-axis and (b) blade height projection on Y axis .....	43
Figure (20) Droplet collection efficiency variation for (a) chord length projection on X-axis and (b) blade height projection on Y-axis.....	44
Figure (21) Ice shapes at different flow angles of attack: (a) $-4^\circ$ , (b) $-2^\circ$ , (c) $0^\circ$ , (d) $2^\circ$ (e) $4^\circ$ and (f) $6^\circ$ .....	48
Figure (22) Numerically predicted ice shapes for different icing conditions at (a) LWC = $0.5 \text{ g/m}^3$ , $T = -4^\circ\text{C}$ , (b) LWC = $1 \text{ g/m}^3$ , $T = -4^\circ\text{C}$ , (c) LWC = $0.5 \text{ g/m}^3$ , $T = -8^\circ\text{C}$ and (d) LWC = $1 \text{ g/m}^3$ , $T = -8^\circ\text{C}$ .....	51
Figure (23) Computational grids around airfoils with accreted ice for different icing conditions: (a) LWC = $0.5 \text{ g/m}^3$ , $T = -4^\circ\text{C}$ , (b) LWC = $1 \text{ g/m}^3$ , $T = -4^\circ\text{C}$ , (c) LWC = $0.5 \text{ g/m}^3$ , $T = -8^\circ\text{C}$ and (d) LWC = $1 \text{ g/m}^3$ , $T = -8^\circ\text{C}$ .....	54
Figure (24) Aerodynamic performance for predicted ice shapes, in terms of (a) lift coefficient and (b) drag coefficient.....	55
Figure (25) Ice accretion on NACA 0012 obtained numerically using LEWICE (dashed line) and experimentally (solid line) [47] .....	57
Figure (26) Accretion shapes on NACA 0012 modeled by FENSAP ICE for comparison....	57

## Nomenclature

### Symbols:

$\rho$	Density (kg/m <sup>3</sup> )
$V$	Velocity (m/s)
$T$	Static temperature (K)
$m$	Mass flow (kg)
$d$	Droplet diameter ( $\mu\text{m}$ )
$A$	Surface area (m <sup>2</sup> )
$\sigma_{ij}$	Stress tensor
$p$	Static pressure (Pa)
$\mu$	Dynamic viscosity (kg/m s)
$E$	Internal energy (J)
$H$	Enthalpy (J/kg)
$\alpha$	Local water volume fraction (kg/m <sup>3</sup> )
$\beta$	Collection efficiency
$C$	Chord length (m)
$C$	Coefficient
$F$	Force (N)
$K$	Droplet inertia parameter
$\tau_{ij}$	Shear stress tensor
$g$	Gravity vector (m/s <sup>2</sup> )
$F_r$	Froude number
$Re$	Flow Reynolds number
$L$	Latent heat (J/kg)

$Q$	Heat flux ( $\text{W}/\text{m}^2$ )
$\sigma$	Boltzmann constant ( $\sigma = 5.67 \times 10^{-8} \text{ W}/\text{m}^2\text{K}^4$ )
$\varepsilon$	Solid emissivity
$n$	Surface normal vector
$X_{\text{Offset}}$	Offset distance (m)
$T_{\text{Max}}$	Maximum thickness (m)
$X_{\text{Mean}}$	Average distance (m)

### **Superscripts:**

$a$	Air
$d$	Droplet
$f$	Fluid
$evap$	Evaporation
$s$	Solid
$^\circ$	degree
$\infty$	Reference or freestream
$rec$	Recovery
$h$	Water film height
$l$	Lift
$d$	Drag
U	Upper
L	Lower

### **Abbreviations:**

LWC	Liquid water content
MVD	(Droplet) Median volumetric diameter
CFD	Computational fluid dynamics

HAWTs Horizontal axis wind turbines

NREL National Renewable Energy Laboratory

AoA Angle of attack

# **Chapter 1 Introduction**

## **1.1. Background**

Wind turbines are increasingly prevalent in the global generation of renewable energy [1]. Wind turbines are a promising technique to reduce diesel power generation in remote communities such as Newfoundland and Labrador; however, the wind conditions in cold and harsh environments create several problems for the performance, longevity and safety of a wind turbine installation. High quantities of ice accretion, precipitation, unsteady wind conditions and limited accessibility are significant challenges to wind power development. Precipitation impacts the blade's leading edge and diminishes system performance by deteriorating the blade surface which creates rotational imbalance, structural vibrations and auditory noise output. Ice accretion on the turbine blades can significantly reduce performance and the useful life of a turbine by changing the airfoil profile and weight balance, as well as increase overall blade weight. This research program investigates icing on wind turbine numerically to better enable wind turbines in cold and harsh environments.

## **1.2. Research Objectives**

This thesis analyzes the gas-solid and gas-liquid flows that cause ice accretion on a turbine blade and the corresponding effect on aerodynamic performance. Ice accretion rates on turbine blade surfaces are numerically modeled and predicted. Modeling and simulations are performed using a workstation computer and commercially available

CFD software. The research objectives also aim to investigate the basic ice accretion variables including atmospheric temperature, blade surface roughness, LWC, MVD, blade design / curvature and relative angle of attack.

### **1.3. Thesis Organization**

This thesis is organized into five chapters. In Chapter 2, a foundational overview of wind turbine icing is presented. The chapter gives an introduction on cold region environments, ice growth physics and mechanisms, ice accretion effects on wind turbines, and a literature review on wind turbine icing. In Chapter 3, the methodology of ice accretion simulation / modeling on wind turbine blade is presented. The chapter provides details on the computational grid, multi-phase flow equations formulation, and describes two useful approaches for ice modeling by FENSAP-ICE. In Chapter 4, the results and discussions of different studies are presented. The chapter investigates the effects of many icing factors on wind turbine blade. In Chapter 5, conclusions of the thesis work are presented. The chapter summarizes this research work and provides suggestions for future research.

## **Chapter 2 Literature review**

### **2.1. Wind Power in Cold Regions**

Cold climate regions are often strong locations for wind power utilization in high latitudes of Eastern and North Europe, North America and Asia [2]. Cold climate regions can be classified into conventional sites which refer to sites located in exposed and windy areas that are characterized by temperate weather, and nonconventional sites which refer to sites that are characterized by wet and stormy climate areas. Non-conventional sites exhibit the following characteristics: an air temperature below 0°C for long periods during the year, complex terrains which are characterized by site elevations up to 800 m above sea level, clouding approximately at a low ground surface level in which high water content, precipitation and sprays from atmosphere and / or seawater and extreme conditions such as high turbulence due to extreme wind speeds, as well as snow storms [2, 3]. Canada is one of the most abundant sources of wind power, with seventh largest installed capacity (world-wide).

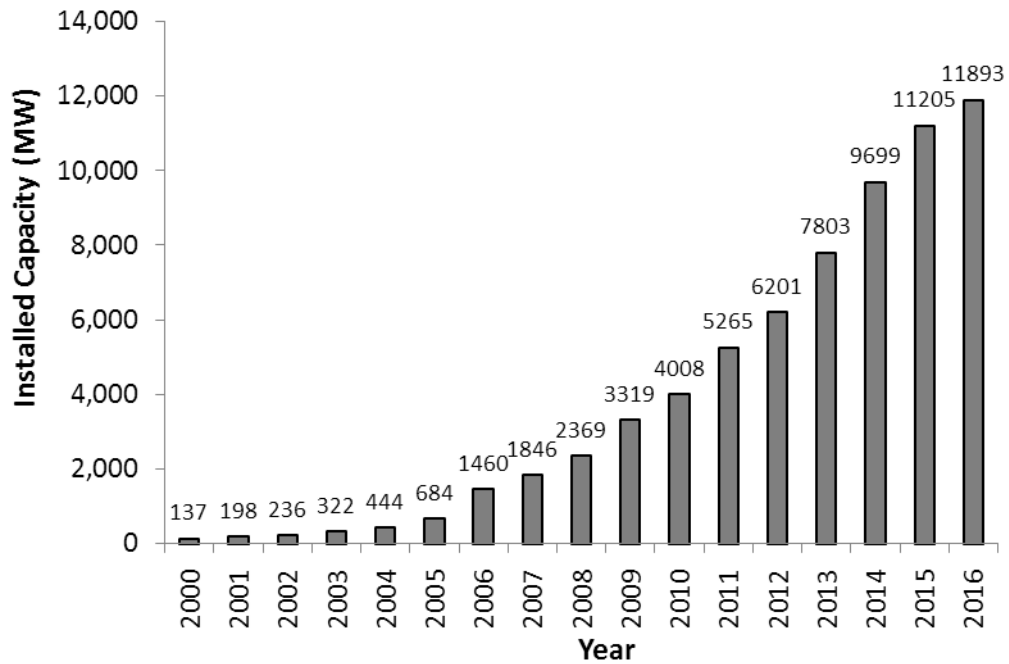


Figure (1) Canada installed wind capacity over last 16 years taken from CANWEA, 2017

As illustrated in Figure (1), as of 2016, the total installed capacity reached 11,898 MW. According to the National Energy Board data, wind energy in Canada supplies approximately 6% of its total electricity demand [4].

## 2.2. Icing Effects on Wind Turbines

Typically, ice accretion on rotor blades or other wind turbine components can have significant impacts on its operation (aerodynamics [5], control system, material response and vibrations), safety (ice throwing [6], noise, site accessibility) and economics (energy harvest, decreased turbine lifespan [6] and necessary ancillary equipment) [7]. A variety of icing problems on wind turbines have been reported, including a significant loss of power production [8, 9]. The loss in power is due to the disrupted aerodynamics, overloading and increased fatigue of components [8, 10].

### 2.3. Ice Growth on Wind Turbines

Typically, ice growth on wind turbine blades can be classified into three different situations: during power generation, during idling (in which the blades are rotating but no power generated to the grid) and standstill (in which the rotor is locked and at rest).

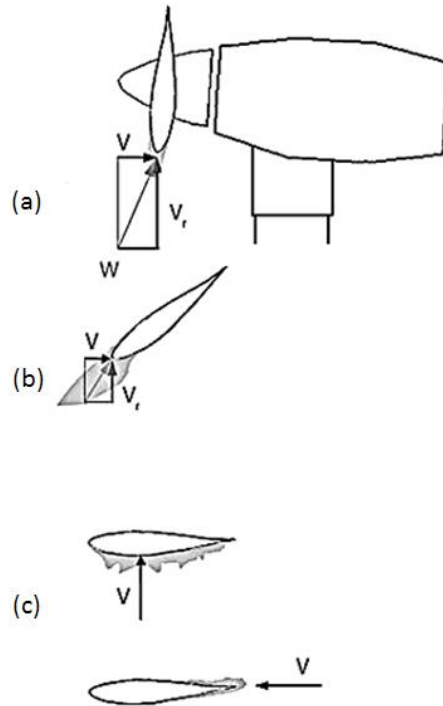


Figure (2) Ice growth configurations on a pitch controlled wind turbines (a) power generation, (b) idling, and (c) standstill modified from Battisti et. al. 2015

As illustrated in Fig. 2, during power generation, the blade rotational speed causes centrifugal forces on the ice structures at the blade leading edge. Combination of these forces with the aerodynamic forces cause shear forces and bending moments between the ice structures and the blade body, resulting in an early removal of formed ice cups. During idling, in which situation the turbine is running at low rotational speed and is

disconnected from the grid or out of gear and the pitch angle is almost close to zero preparing for standstill situation [2]. In HAWTs, due the conjugate effect of increasing relative wind velocity along blade span and chord reduction along blade radius, ice accretion is mainly formed at the outer side of the blade with almost linear increase towards the tip. Formed ice on the outer side breaks off and continues to grow again during storms forming a typical saw-tooth shape. During standstill, since this situation is approximately like idling but different wind direction, ice location on the blade is mainly affected by wind direction. Consequently, ice mitigation strategies applied on blade leading edge region can be totally ineffective during this situation, as ice accretion on blade trailing edge region could be possible [2].

#### **2.4. Ice Accretion Variables**

Typically, icing variables can be classified into site dependent variables, turbine design dependent variables and other shared variables. Site dependent variables are represented by the climate and metrological conditions of the site including stream atmospheric temperature, pressure, wind speed, liquid water content (LWC), droplet's median volume diameter (MVD), density and relative humidity [11]. Turbine design dependent variables can be represented by rotor blade size, control system (rotational speed) and mitigation or de-icing systems configurations. Other shared variables, including Reynolds number (chord based), heat transfer coefficient, collision efficiency and water impingement area [11].

## **2.5. Ice Accretion Mechanisms on Wind Turbines**

There are three main causes of ice accretion on wind turbine blades: in-cloud icing, precipitation icing and frosty icing. However, precipitation icing and in-cloud icing are the most common types of ice accretion on wind turbines [11].

Precipitation icing is formed by cold / freezing rain or wet snow [12]. The rate of accumulation of this type is usually higher than in-cloud icing. The resulted ice density and freezing rain adhesion are high. Wet snow is partially melted snow crystals with high liquid water content. Wet snow accretion occurs when the air temperature ranges between 0 and -3°C. Its typical density ranges from 200 to 900 kg/m<sup>3</sup> [7, 11]. The wet snow will be frozen when the wet snow accretion is followed by a decrease in temperature. Wet snow is usually risky for its additional weight on standing structures, such as wind turbines in standstill conditions [2].

In-cloud icing occurs when super cooled liquid droplets collide with moving objects and freeze upon impact [13, 14]. In-cloud icing on wind turbines typically has two main types: rime and glaze ice. The type of ice formed on a wind turbine is based on several environmental and operational variables, including temperature, pressure, wind velocity, liquid water content (LWC), median volume diameter of droplets (MVD), blade geometry, roughness, heat flux, icing time, droplets impingement area and collection efficiency [2]. Prediction of both type and shape of ice during an icing event can be difficult due to the rapid changes in the atmospheric conditions. Depending on the atmospheric temperature range, different types and shapes of ice can be formed [15].

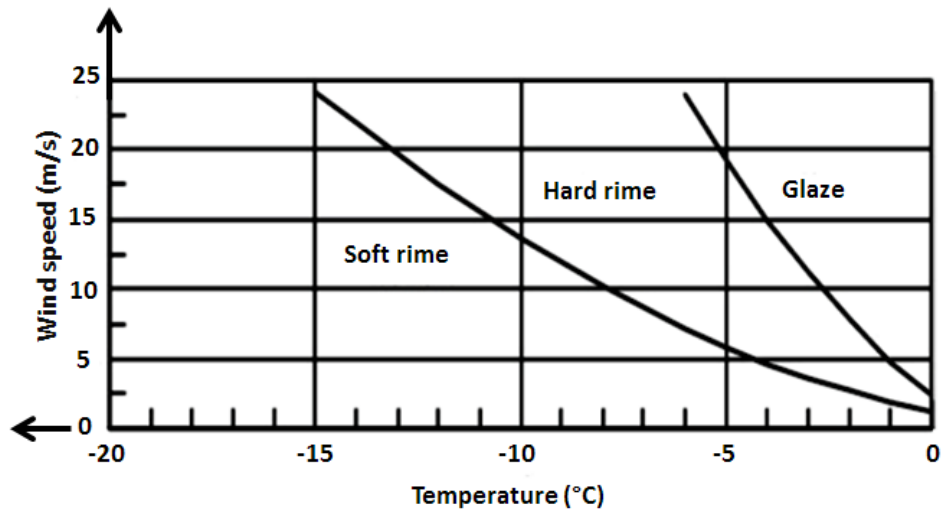


Figure (3) Empirical relationship between ice type, wind speed and temperature by Fikke et. al. 2006

As illustrated in Fig. 3, icing typically occurs between 0°C and -15°C [2, 7, 15]. Glaze ice is associated with high quantities of liquid water content, droplet diameter ranges from 0 µm to 500 µm and temperatures ranges from 0°C to -5°C [2, 7]. A transparent ice layer cap with a density near to 900 kg/m<sup>3</sup> is often associated with glaze ice accretion [2, 7]. Rime ice is typically associated with frozen fog with small droplet sizes, ranging from 0 µm to 10 µm. It usually occurs at temperatures below -5°C. Its density can range from 100 kg/m<sup>3</sup> to 600 kg/m<sup>3</sup> [2, 7].

Atmospheric measurements show that LWC varies from 0 g/m<sup>3</sup> to 5 g/m<sup>3</sup>. In stratiform clouds, LWC rarely exceeds 1 g/m<sup>3</sup>, however, higher quantities can exist in cumuliform clouds [2, 16]. The relationship between LWC, MVD and temperature was experimentally evaluated showing that LWC decreases as the droplet size increases [17].

It was also observed that LWC decreases with altitude and temperature [16, 18].

Stratiform clouds are characterised by a lower range of droplet sizes than that of cumuliform clouds. Both cloud types have droplet sizes up to 50  $\mu\text{m}$  [16, 17, 18].

## **2.6. Ice Accretion mitigation strategies on Wind Turbines**

Typically, the most common technologies used for de-icing and anti-icing systems are electro-thermal technologies because of their simplicity and high efficiency. Heating elements for thermal strategies are integrated into the blade impacting the structural integrity and sometimes lead to blade delamination. The power used for de-icing and anti-icing systems ranges from 2% to 15% of the turbine's output power; depending on severity, time-span and quantity of icing events, as well as the size of the wind turbine. Ice accretion rate on large wind turbines is less than small wind turbines which represents less consumed energy by proportion. To decrease power consumption, the layout of heating elements on the blade surface is very important [19]. De-icing techniques are less expensive compared to anti-icing. De-icing minimizes runback water and refreezing water in unheated areas allowing some ice layers to be formed on the blade surface. For anti-icing systems, no ice is accumulated. Many technologies are available to de-ice on wind turbine blades, such as electro-thermal [20], electro-repulsive or piezoelectric, hot air flow, microwave, icephobic and pneumatic boots coatings, among others. The best position for an ice detector used to activate the de-ice or anti-icing systems is at the leading edge of blade tip. This is because of the high relative speed at the tip, which causes the blade tip to collect more water and accrete

more ice than other sections of the blade. During anti-icing mode, it is important to provide the energy to maintain blade surface temperature above freezing and to melt ice forming when super-cooled droplets freeze upon impact.

## **2.7. Ice Accretion Investigation on Wind Turbines**

There are two main fields of investigation of icing on a wind turbine rotor blade. The first one is analysing the aerodynamic impacts of a given ice shape accreted on rotor blade such as prediction of lift and drag characteristics. The second one is on the capability to capture the resulted ice shapes for specific atmospheric conditions, experimentally using wind tunnels or numerically by modeling and simulations.

Experimentally, it is difficult to reproduce tests in wind tunnels to examine icing effect because of the dimension constrains, scaling problems, and rotor rotation constraints. Numerically, several ice accretion solvers have been developed to predict inflight icing on aircrafts including flight tests, experimental simulation [21, 22], engineering methods [23] and numerical simulations [24, 25]. These solvers have common methodologies in predicting heat transfer, water droplet impingement and ice accumulation. The most commonly used solvers that can be used to investigate icing on wind turbines are LEWICE from NACA USA [26], LEWICE is 2-D an ice accretion code developed by NASA Glenn Research Center. The code applies a time-stepping procedure code to predict ice accretion shape. The flow field calculations are computed using Douglas Hess-Smith 2-D panel code. Then the obtained solution is used to calculate the trajectories of particles and impingement points on the body. The icing model is then

used to predict the ice growth rate and shape [18]. TURBICE (Turbine Blade Icing Model), from the Technical Research Centre of Finland, is a two-dimensional ice accretion simulation program. It was developed to predict icing on wind turbine blades. TURBICE uses panel methods to calculate potential flow field around the blade. The program uses Lagrangian technique for droplet trajectories and impingement calculations. The program is capable of calculating collision efficiencies and locating the droplet impingement locations along the blade surface. The program can estimate the amount of energy required for heating to prevent ice accretion on a blade surface [27 - 29]. FENSAP ICE, for 3D modeling from Numerical Technologies International is a 3-D in-flight icing simulation solver. The solver simulates flow field, droplet impingements, ice shapes and predicting anti/de-icing heat loads using a built in CFD modules. It uses 3D Navier-Stokes and energy equations for flow field calculations and 3-D Eulerian model for droplet calculations [30 - 32]. It is a leading CFD program to predict ice accretion on wind turbine blades .

A numerical investigation on the relation between icing temperature and turbine size indicated that icing can be more severe for small wind turbines in terms of aerodynamic disturbance [33]. Other numerical studies indicated that rotor angular speed has a major impact on the ice quantity and ice load increases with blade span [33, 34]. Furthermore, ice is mostly formed on the leading edge of the blade section [35, 36].

Performance of wind turbines primarily depends on the wind speed and blade aerodynamics. The roughness generated due to ice accretion can significantly affect

aerodynamics and reduce power output. The reduction in torque due to ice is greater for small wind turbines compared to large wind turbines. Ice accretion on a wind turbine blade causes a significant change in aerodynamic characteristics [37]. Typically, there is a linearly proportional reduction in lift coefficient and increase in drag coefficient. Mixed ice formation (glaze and rime) causes the largest flow separation and hence more lift degradation is expected [38, 39].

Ice accretion shape is significantly affected by the operating conditions of the wind turbine [25]. Streamlined ice shapes were observed at lower temperatures and horn ice shapes at higher temperatures [40]. One numerical study [41] showed that ice shape has significantly more impact on power reduction than ice thickness on the turbine blades [41]. A study investigating icing on NREL Phase VI rotor using FENSAP-ICE [42] showed that power loss can be up to 60% for certain conditions, with the largest losses in lower wind velocities. Results indicated that glaze ice on the rotor blades causes a greater power loss than rime ice, as glaze ice can correspond to greater ice thickness and an increased icing surface [42]. At high wind speeds and specific icing conditions, certain ice shapes can cause an unanticipated increase in aerodynamic performance [37, 42].

Ice growth rate increases with increasing droplet size. Ice mass along the blade span can be varied due to the effect of centripetal forces, gravity, and cross flow over the blades. Centripetal force affects the water droplets impingement causing a greater building up of ice at the blade tip [36]. In a numerical analysis investigating ice accretion on five different sections of blade span indicated that icing is less severe near the blade

root section [13]. Combined changes in blade section length and relative wind velocity that correspond to blade span considerably influence the physics of ice accretion.

Current wind turbine hub height can reach up to 135 m, and blade tip height can reach 200 m above the ground. Atmospheric icing conditions mainly depend on the surrounding environment. Lowest cloud extent can be at 480 m above sea level for cumuliform clouds and more than 1 km for stratiform clouds. LWC changes with altitude. By the assumption of no significant change in quantities of LWC and MVD at turbine tower height compared to cloud extent, wind turbines can experience in-cloud icing [2]. Since Meteorological data at lower altitudes (wind towers) are not available therefore different icing conditions with higher and lower LWC concentrations can be numerically predicted using cloud characteristics if in cloud icing conditions is occurred.

This research work aims to predict the effect of LWC / MVD, at different temperatures, on ice mass. Ice accretion on wind turbines is investigated in terms of airfoil type and blade thickness, as well as its effect on aerodynamic performance. All profiles of NREL airfoil families are investigated to provide insights on the effect of airfoil design parameters on ice accretion. Variable blade thickness is useful to investigate ice accretion physics at different locations along a wind turbine's radius, as typical turbine designs often have varying airfoil thickness from the blade's root to tip. Lastly the effect of different ice shapes at different flow angle of attack, caused by differing icing conditions, on aerodynamic performance provides important insights for wind turbine design and placement strategies.

## Chapter 3 Methodology

To develop the model, the geometry of the blade and surrounding domain, as well as the grid discretizations, are created using “ANSYS Design Modular”, a commercial software. The grid file is exported to FENSAP ICE solver. The procedure for ice modeling in FENSAP ICE consists of three steps which are flow field, droplet and ice calculations. The iced airfoil grids used for prediction of aerodynamic characteristics due to ice are obtained using a built-in mesh displacement tool in FENSAP ICE. The 3D FENSAP ICE solver has been successfully used for wind turbine icing simulations [41].

### 3.1. Mesh Discretization Scheme

The NREL airfoil families are selected to investigate icing as they are widely used for HAWTs blade industry [43]. For all airfoils, a chord length of 1 m is maintained along a blade span of 0.25 m to represent a small portion of a rotor blade. A fine 3D structured grid is created for each airfoil with identical discretization schemes. For a NREL S809 profile (Fig. 4), a fine 3D structured grid with 34,823 cells is created with a minimum orthogonal quality of 0.835 (where values close to 0 correspond to low quality and 1 represents high quality) and maximum orthogonal skew of 0.194 (where values close to 1 correspond to low quality and 0 represents high quality). The grid’s first boundary layer thickness is  $1 \times 10^{-6}$  m with a growth rate of 1.1 for 135 layers to accurately capture ice shape and mass on blade surface. The main advantages of using a structured grid are higher resolution and better accuracy. The structured domain uses hexahedra cells

which are characterized by regular connectivity and efficient spacing. As shown in Fig. 5a, a circular domain (O grid type) with a diameter of 20 m is created. Ice accretion is mostly formed at the leading edge due to flow stagnation. Smaller elements are created at the leading edge with equal spacing of 0.001 m to accurately evaluate both ice mass and shape. The cell size gradually changes along the airfoil surface, as illustrated in Fig. 5b.

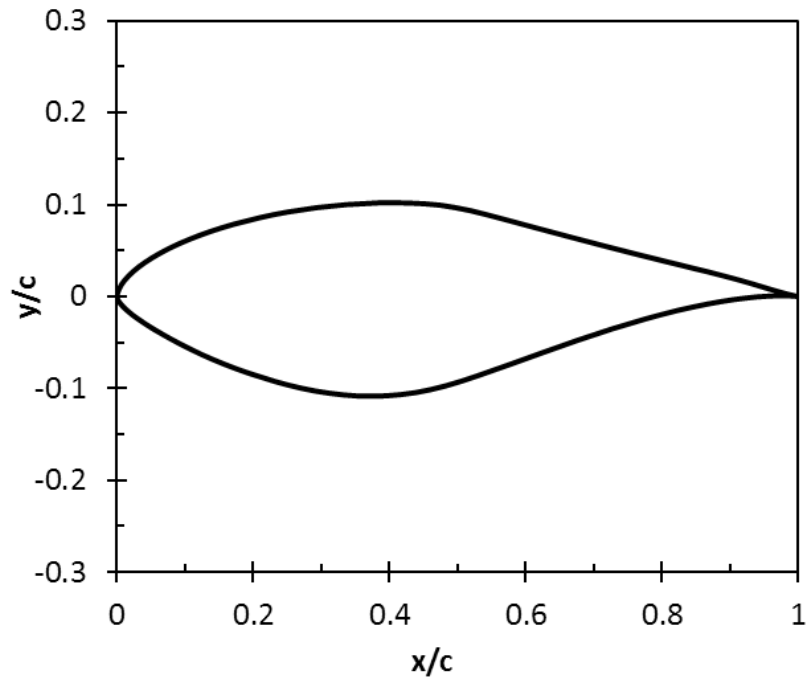
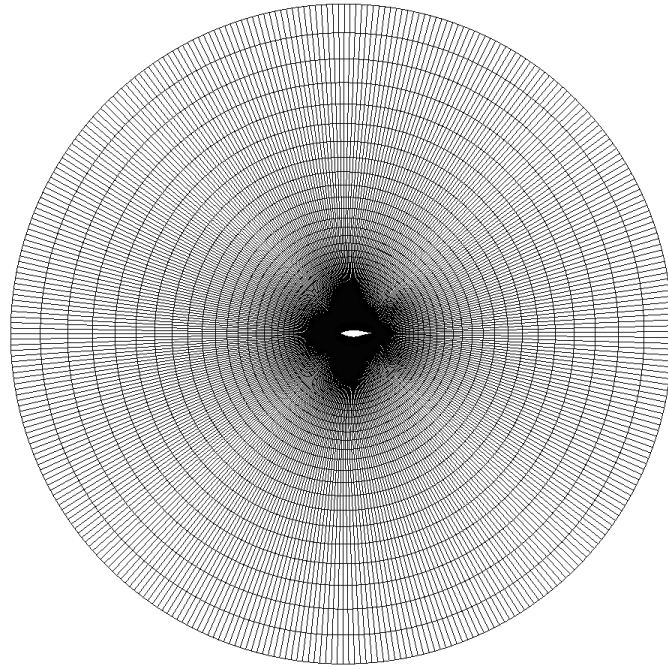
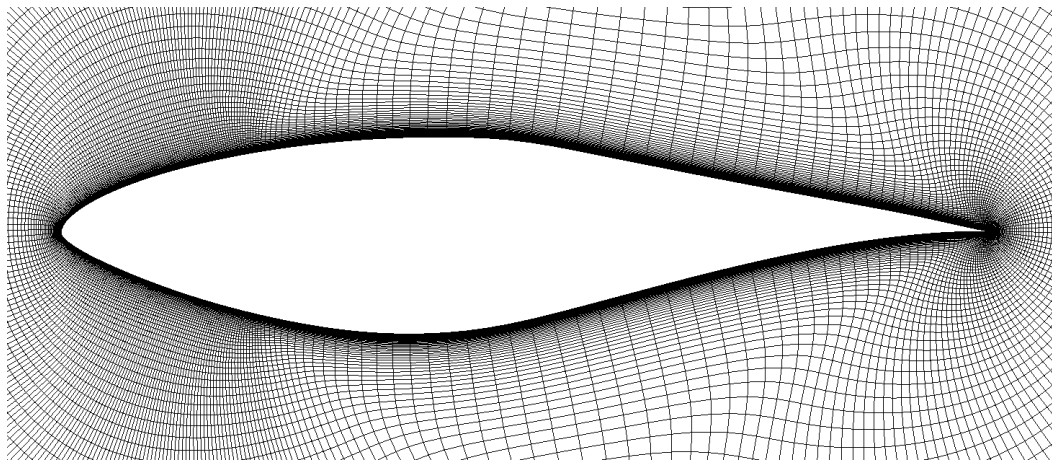


Figure (4) NREL S809 airfoil profile



(a)



(b)

Figure (5) Grid discretizations for (a) elevation view of O grid and (b) cell distribution around the blade

### 3.2. Formulation of Multiphase and Phase Change

Typically, the numerical simulation of ice accretion mainly consists of the following modules: air flow solution, droplets collection efficiency calculations, evaluation of boundary layer characteristics, and ice mass evaluation by thermodynamic model computation [44].

#### Flow field calculations

The air flow solution is solved by FENSAP solver with the 3D Navier-Stokes and energy equations [45]. The Navier-Stokes equation is expressed as

$$\frac{\partial \rho_a \vec{V}_a}{\partial t} + \vec{\nabla} \cdot (\rho_a \vec{V}_a \vec{V}_a) = \vec{\nabla} \cdot \sigma_{ij} + \rho_a \cdot g \quad (1)$$

where  $\rho_a$  is the air density and  $V_a$  is the velocity vector. The stress tensor,  $\sigma_{ij}$ , is represented by

$$\sigma_{ij} = -\delta_{ij} p_a + \mu_a \left( \delta_{jk} \nabla_k v_i + \delta_{ik} \nabla_k v_j - \frac{2}{3} \delta_{ij} \nabla_k v_k \right) = -\delta_{ij} p_a + \tau_{ij} \quad (2)$$

where  $p_a$  and  $\mu_a$  represent air static pressure and dynamic viscosity of air, respectively.

The conservation of energy equation is

$$\frac{\partial \rho_a E_a}{\partial t} + \vec{\nabla} \cdot (\rho_a \vec{V}_a H_a) = \vec{\nabla} \cdot [K_a (\vec{\nabla} T_a) + v_i \tau_{ij}] + \rho_a \vec{g} \cdot \vec{V}_a \quad (3)$$

where E and H are the total internal energy and enthalpy, respectively. The airflow around a blade is typically turbulent at high Reynolds numbers, thus one-equation Spalart Allmaras turbulence model is used [46]. The heat fluxes at the blade wall are

computed with second order accuracy by solving the energy equation. Lift and drag coefficients can be calculated from

$$C_l = \frac{2F_l}{\rho_{a,\infty} V_{a,\infty}^2 A_\infty} \quad (4)$$

$$C_d = \frac{2F_d}{\rho_{a,\infty} V_{a,\infty}^2 A_\infty} \quad (5)$$

where  $F_l$  and  $F_d$  are lift and drag forces, respectively, and  $A_\infty$  is the reference surface area (based on  $C$ , chord length and blade span-wise length).

### Droplet calculations

Water concentration, droplet velocity vectors, collection efficiency, impingement, shadow zone properties and impingement limits over the entire domain are provided by the DROP 3D solver [45]. The general Eulerian two-fluid model is used, which consists of the Euler or Navier-Stokes equations augmented by the droplets continuity and momentum equations,

$$\frac{\partial \alpha}{\partial t} + \vec{\nabla} \cdot (\alpha \vec{V}_d) = 0 \quad (6)$$

$$\frac{\partial (\alpha \vec{V}_d)}{\partial t} + \vec{\nabla} (\alpha \vec{V}_d \otimes \vec{V}_d) = \frac{C_D R_{ed}}{24K} \alpha (\vec{V}_a - \vec{V}_d) + \alpha \left(1 - \frac{\rho_a}{\rho_d}\right) \frac{1}{Fr^2} \quad (7)$$

where  $\alpha$  and  $V_d$  are water volume fraction and droplet velocity, respectively. The first term in the momentum equation represents the drag on a droplet with MVD. The

second term represents the buoyancy and gravity forces. The droplet distribution is set as mono-disperse which indicates a calculation performed for a single diameter of droplets.

### Icing calculations

The ICE 3D solver uses mass conservation and energy conservation equations to solve complex thermodynamics of ice formation [45]. The equation expressing mass conservation is

$$\rho_f \left[ \frac{\partial h_f}{\partial t} + \vec{\nabla} \cdot (\vec{V}_f h_f) \right] = V_\infty LWC\beta - \dot{m}_{evap} - \dot{m}_{ice} \quad (8)$$

where  $f$  and  $\beta$  represent water film and collection efficiency, respectively. The first term represents the mass of water impingement, the second term is mass of evaporated water and the third term is ice mass. The conservation of energy equation is

$$\begin{aligned} & \rho_f \left[ \frac{\partial h_f c_f \tilde{T}_f}{\partial t} + \vec{\nabla} \cdot (\vec{V}_f h_f c_f \tilde{T}_f) \right] \\ &= \left[ c_f (\tilde{T}_\infty - \tilde{T}_f) + \frac{||\vec{V}_d||^2}{2} \right] V_\infty LWC\beta - L_{evap} \dot{m}_{evap} \\ &+ (L_{fusion} - c_s \tilde{T}) \dot{m}_{ice} + \sigma \varepsilon (T_\infty^4 - T_f^4) - c_h (\tilde{T}_f - \tilde{T}_{ice,rec}) \\ &+ Q_{anti-icing} \end{aligned} \quad (9)$$

where  $\rho_f, c_f, c_s, \varepsilon, \sigma, L_{evap}$  and  $L_{fusion}$  represent the physical properties of fluid. The variables  $T_\infty, V_\infty, LWC$  and  $\beta$  represent the airflow and droplets reference parameters. The collection efficiency is calculated by

$$\beta = -\frac{\alpha \bar{V}_d \cdot \vec{n}}{(LWC)V_\infty} \quad (10)$$

where  $\vec{n}$  is surface normal vector. On the right-hand-side of the conservation energy equation, the first three terms represent heat transfer generated by the impinging super-cooled water droplets, by evaporation and by ice accretion, respectively. The last three terms are the radiation, convection and conduction heat fluxes, respectively. From this formulation, 3D ice shape, water film thickness and surface temperature can be predicted. The flow and droplet solutions are input to the ICE 3D solver to predict ice accretion. The icing model uses classical heat flux, which is based on temperature gradients on the walls. Blade wall temperature is maintained a few degrees higher than corresponding adiabatic temperature of flow stream (air and droplets) to obtain meaningful heat fluxes to ICE 3D, since no de-icing strategies are applied (i.e. if the flow's temperature is  $-5^\circ\text{C}$  the blade temperature will be  $-1^\circ\text{C}$ ) [45].

### 3.3. Single and Multi-Shot Approaches

#### Single-shot calculations

For single-shot approach, the sequence of runs are illustrated in Fig. 6. Flow field and droplet solutions are computed once and icing solution is obtained for one interval of time (total icing time), thus no update in the grid, air and droplet solutions during ice formation is represented.

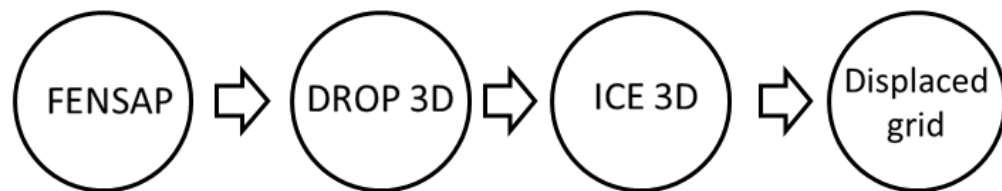


Figure (6) Solution scheme for single-shot approach

#### Multi-shot calculations

For multi-shot approach, the sequence of runs are illustrated in Fig. 7. The total icing time is divided into short time intervals and an icing solution is obtained for each interval. Number of shots means the number of divisions of total icing time. Calculation of the first time interval will predict the first ice layer in terms of mass and shape then output grid / solutions are used as an input to predict second ice layer and the process is continued for each shot. The transient changes in geometry, surface heat fluxes and droplet impingement profile during ice formation are simulated. For an accurate

prediction of ice shape, multi-shot approach better represents the ice conditions. Multi shot calculations are more accurate to simulate ice accretion on an object, especially for heavy ice accretion.

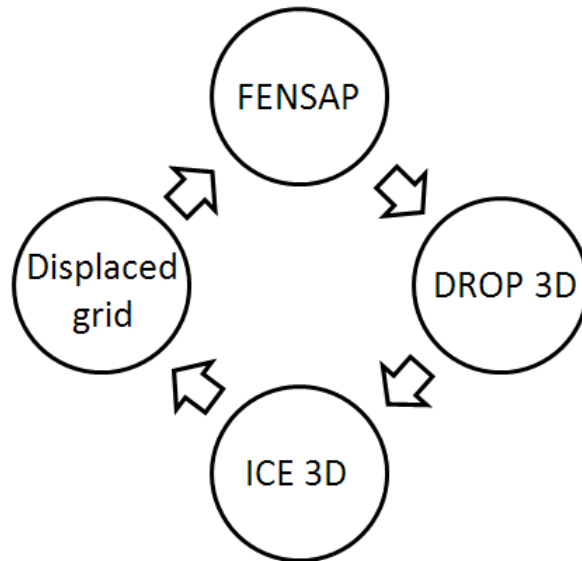


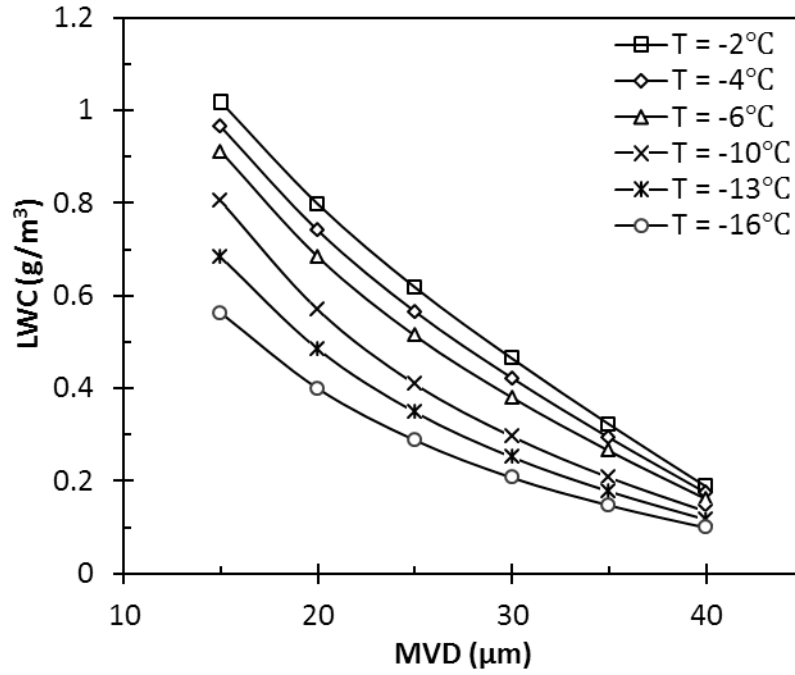
Figure (7) Solution scheme for multi-shot approach

## Chapter 4 Results and Discussions

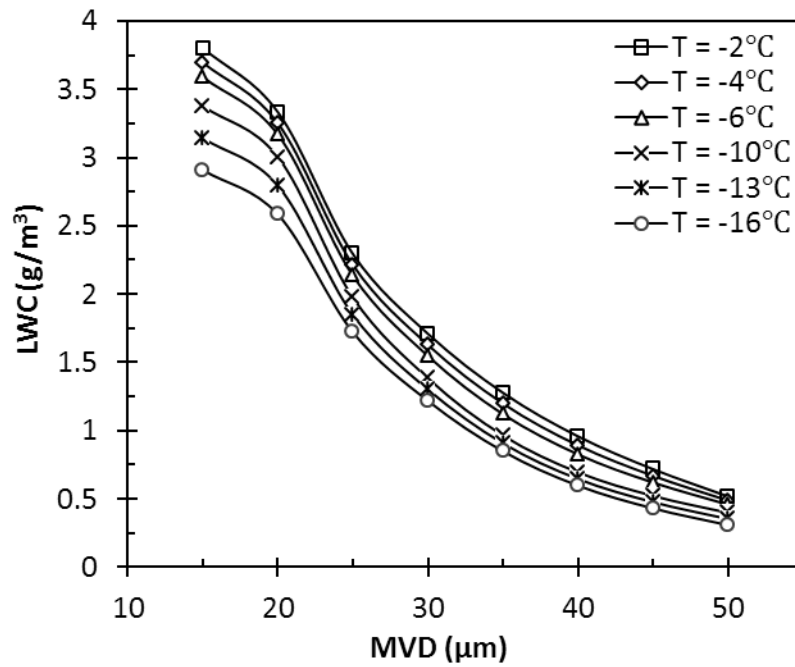
In this section, numerically predicted results of ice accretion rates on wind turbine blade section are investigated in terms of wind velocity, air temperature, LWC, MVD, surface roughness, angle of attack (AoA), blade thickness / curvature parameters and icing time. Wind velocity is maintained at 75 m/s to represent the relative wind speed at 80% of blade span or tip section (estimated for a wind speed of 12 m/s to 15 m/s, a tip-speed-ratio of 6 to 7, a swept area radius of 30 m to 40 m, and a rated power of 0.8 MW to 1.5 MW). Icing times of 3,600 s and 1,800 s are investigated using both single- and multi-shot approaches. Air temperatures of  $-2^{\circ}\text{C}$ ,  $-4^{\circ}\text{C}$ ,  $-6^{\circ}\text{C}$ ,  $-8^{\circ}\text{C}$ ,  $-10^{\circ}\text{C}$ ,  $-13^{\circ}\text{C}$  and  $-16^{\circ}\text{C}$  are investigated. Ice accretion on the wind turbine blade is investigated at different flow angles of attack of  $-4$ ,  $-2$ ,  $0$ ,  $2$ ,  $4$ ,  $6$  degrees.

Numerical predictions of ice accretion shapes at different icing conditions and its effect on aerodynamic performance are presented. Both LWC and MVD values are approximately specified based on the atmospheric conditions. LWC values at each droplet size are obtained using a correction factor estimated by the DROP 3D solver tool box. The correction factor's value depends on cloud extent / height. The lowest possible altitude for each cloud is selected to evaluate the correction value for each cloud type. To obtain LWC values presented in Fig. 8 for both cloud types, the original measured values at high altitudes are multiplied by the obtained correction value to estimate low altitude icing conditions. Icing environment can be characterized by high or low values of LWC. As shown in Fig 8a, stratiform clouds represent an icing environment with lower

LWC, and cumuliform clouds represent an icing environment with higher LWC, as illustrated in Fig. 8b.



(a)



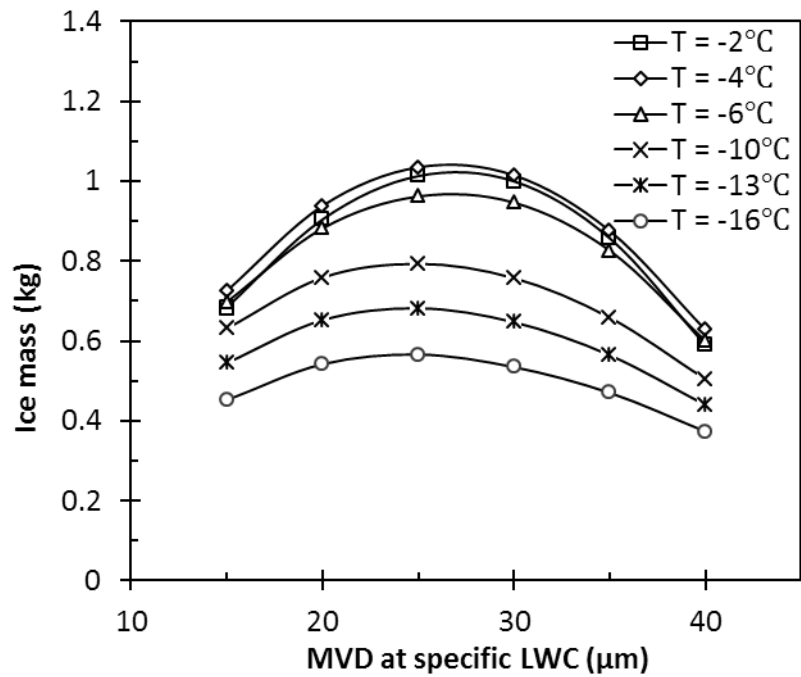
(b)

Figure (8) Variation of LWC with MVD in (a) stratiform clouds and (b) cumuliform clouds.

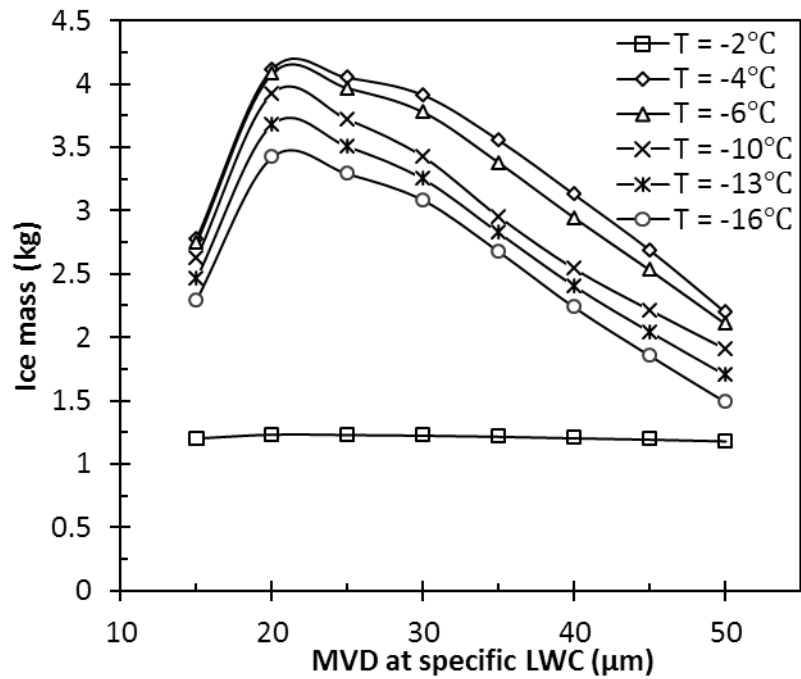
Different icing events are investigated at different temperatures to examine glaze and rime ice loads. The input meteorological conditions shown in Fig. 8 are approximately related to each cloud, thus the relation between LWC and MVD variation at each temperature can be used to study its effect on ice mass.

#### **4.1. Ice Accretion Loads Using Single-Shot Approach**

A flow field solution is computed for each flow temperature and is used as an input for the DROP 3D solver. Each icing condition (LWC and MVD values at specific temperature) is selected from appendix C [16] built in DROP 3D solver. The droplet distribution is maintained as mono-dispersed (i.e., single diameter). Once a droplet solution is evaluated, the files of airflow, droplet, heat flux and surface roughness are transferred to ICE 3D ice accretion solver. An ice solution is developed for 60 minutes of constant icing conditions. Results for icing conditions with low and high quantities of LWC are predicted. As illustrated in Fig. 9, the atmospheric ice quantity decreases with lower temperatures, as lower temperatures are characterized by lower concentrations of LWC. Ice mass reaches its maximum value at  $-4^{\circ}\text{C}$  due to comparatively high values of LWC at this temperature.



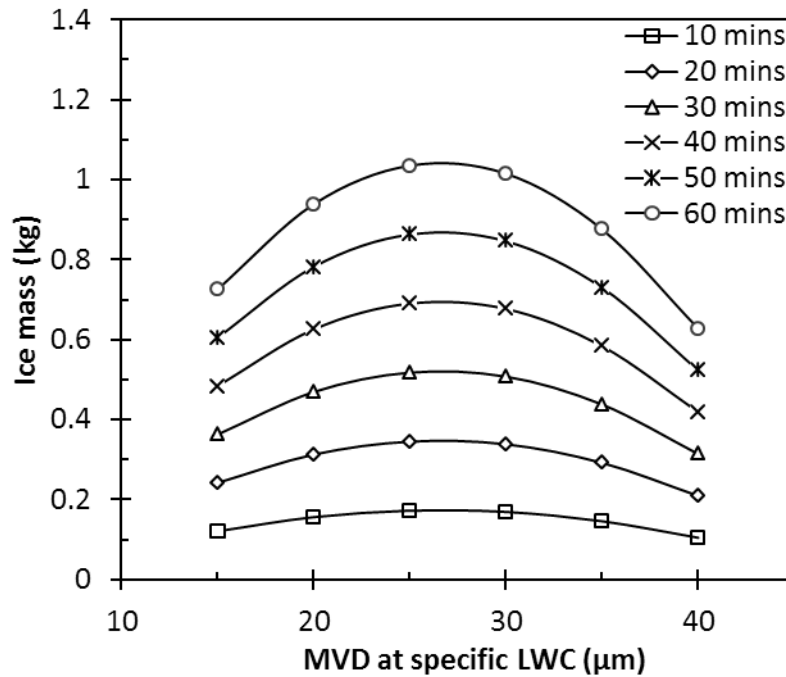
(a)



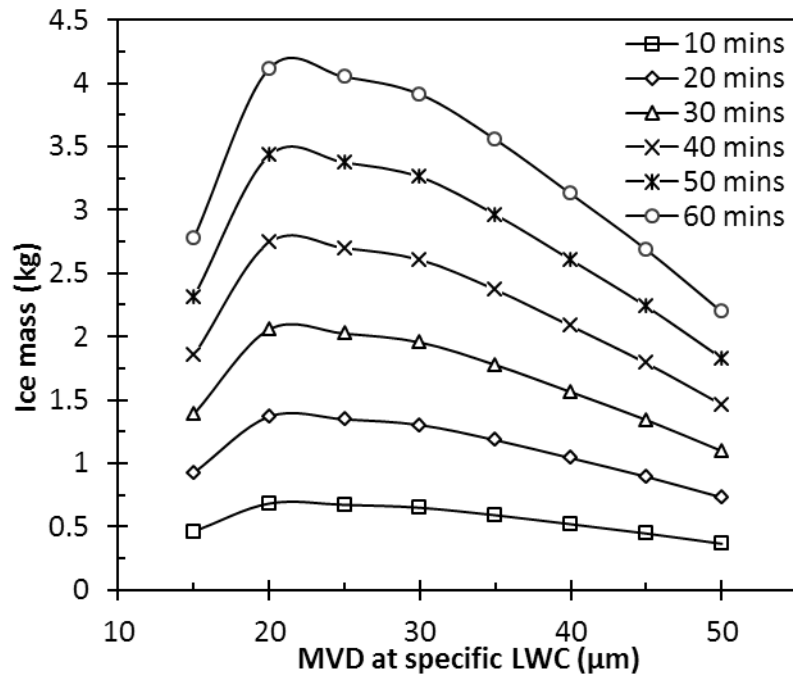
(b)

Figure (9) Ice accretion at several temperatures in (a) low LWC conditions (stratiform clouds) and (b) high LWC conditions (cumuliform clouds)

At  $-2^{\circ}\text{C}$ , high LWC values corresponds to lower ice formation compared to  $-4^{\circ}\text{C}$  due to adiabatic stagnation temperature of the flow. The adiabatic stagnation temperature is determined based on flow speed at a specific atmospheric temperature. Its corresponding value at  $-2^{\circ}\text{C}$  is  $0.8^{\circ}\text{C}$  and at  $-4^{\circ}\text{C}$  is  $-1.2^{\circ}\text{C}$ , hence less ice is formed at  $-2^{\circ}\text{C}$  compared to  $-4^{\circ}\text{C}$ . For MVD from  $20\ \mu\text{m}$  to  $35\ \mu\text{m}$  (at fixed temperature), comparatively high ice quantities can be expected due to the range of droplets at high LWC concentrations. The decrease in mass quantity with temperature for each cloud conditions is consistent as its value mainly depends on LWC. Since the results show that maximum ice is accumulated at  $-4^{\circ}\text{C}$ , this temperature is selected for other studies. Ice accretion versus time is obtained during single shot at  $-4^{\circ}\text{C}$ .



(a)



(b)

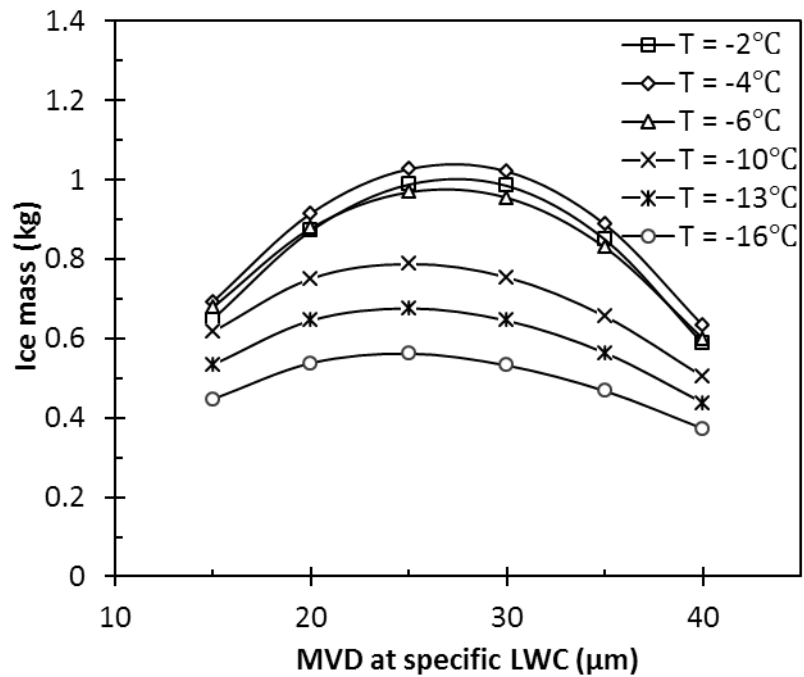
Figure (10) Ice mass variation with time in (a) low LWC conditions (stratiform clouds) and (b) high LWC conditions (cumuliform clouds)

As shown in Fig. 10, for shorter icing times, ice mass does not change noticeably, however, other conditions are varied. Therefore, variation of both LWC and droplet size can affect ice mass during long intervals of icing time.

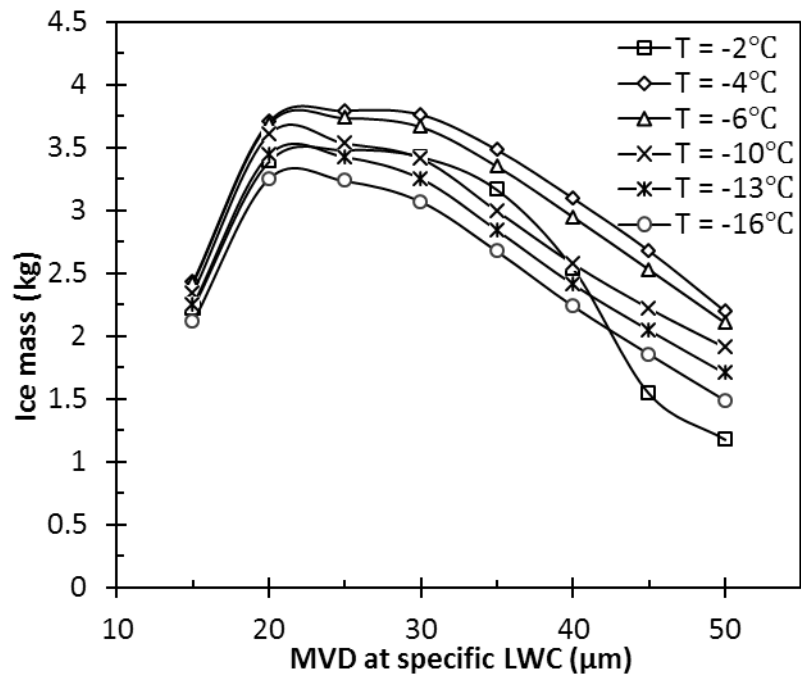
#### 4.2. Roughness Effect on Ice Accretion

To examine surface roughness effect on ice mass, a sand grain roughness model using shin et al. [47] is used to provide a roughness value based on LWC and MVD quantities, to represent blade surface roughness (formed coating) formed based on the environmental conditions prior to an icing event. The LWC magnitude significantly affects roughness as cumuliform clouds conditions can generate higher roughness values

than stratiform clouds. Applied roughness values in this study vary from 0.00042 m to 0.0048 m in stratiform clouds and from 0.0034 m to 0.043 m in cumuliform clouds. Roughness values at lower temperatures are small due to lower LWC concentrations. Both conditions are investigated with applied roughness conditions on the blade surface. As shown in Fig. 11a, results indicate slightly decreasing ice quantities when compared to no roughness. However, as shown in Fig. 11b, for  $-2^{\circ}\text{C}$  (High LWC / cumuliform cloud conditions), there are significant increases in ice accumulation. Roughness can increase ice accretion at higher temperatures (around  $-2^{\circ}\text{C}$ ) with higher LWC conditions. For temperature ranges between  $-4^{\circ}\text{C}$  and  $-16^{\circ}\text{C}$ , surface roughness can result for lower ice accumulation.



(a)



(b)

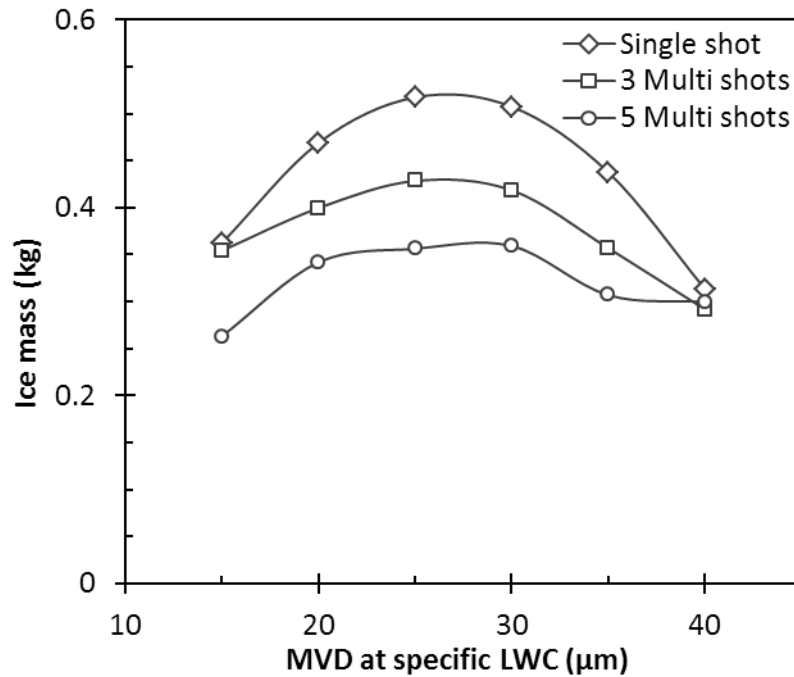
Figure (11) Ice accretion at different temperatures with applied surface roughness for (a) low LWC conditions (stratiform clouds) and (b) high LWC conditions (cumuliform clouds)

### 4.3. Ice Accretion Loads Using Multi-Shot Approach

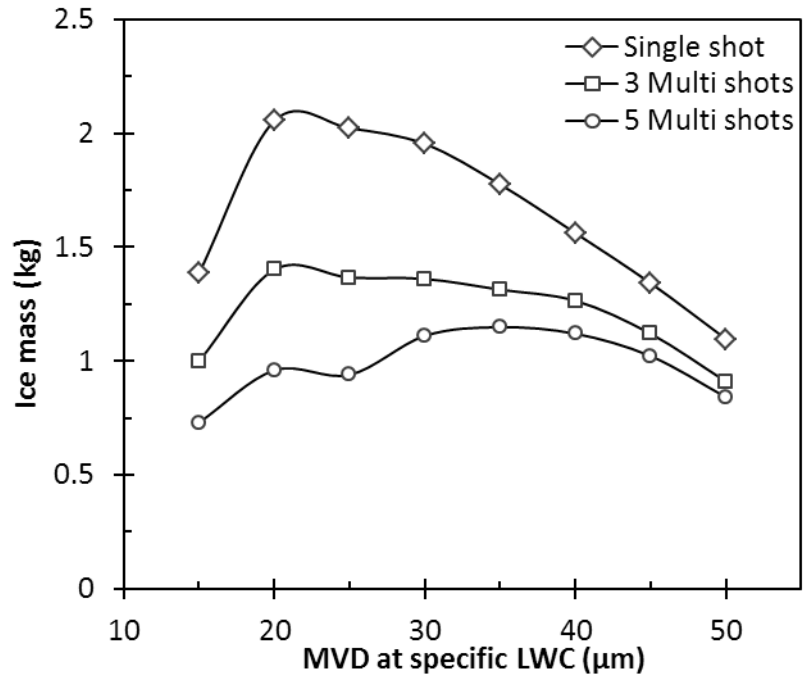
As ice grows on a blade surface, aerodynamics change significantly, affecting flow field, shear stresses, heat fluxes, and droplet collection efficiency. Multi-shot approach accounts for the transient changes during ice accumulation. This not only accounts for the change in the aerodynamics, but also updates the geometry of the surfaces to more accurately predict the total mass of impinged droplets. Multi-shots of ice are computed for 1,800 s at -4°C for both atmospheric conditions. The total time is divided into short intervals of time depending of the number of shots (i.e. time interval for 3 shots equals 600 s). The effect of number of shots effect on ice quantity is investigated for two cases: with and without roughness conditions. A comparison between single, 3 shot and 5 shot

predictions are presented in this section. As shown in Fig. 12, the majority of solutions predict a decrease in ice mass with increased number of shots. For applied roughness conditions, ice mass shows lower reduction percentage in ice quantity compared to no roughness conditions (smooth blade), as illustrated in Fig. 13. Therefore, roughness conditions due to environment can affect (decrease) ice formation process.

For ice multi shot computations, it is computationally difficult to predict ice accretion behaviour in terms of ice mass and shape. More shots leads to accurate computation of ice shape and mass (i.e. as an icing event can be represented by immense quantity of shots).

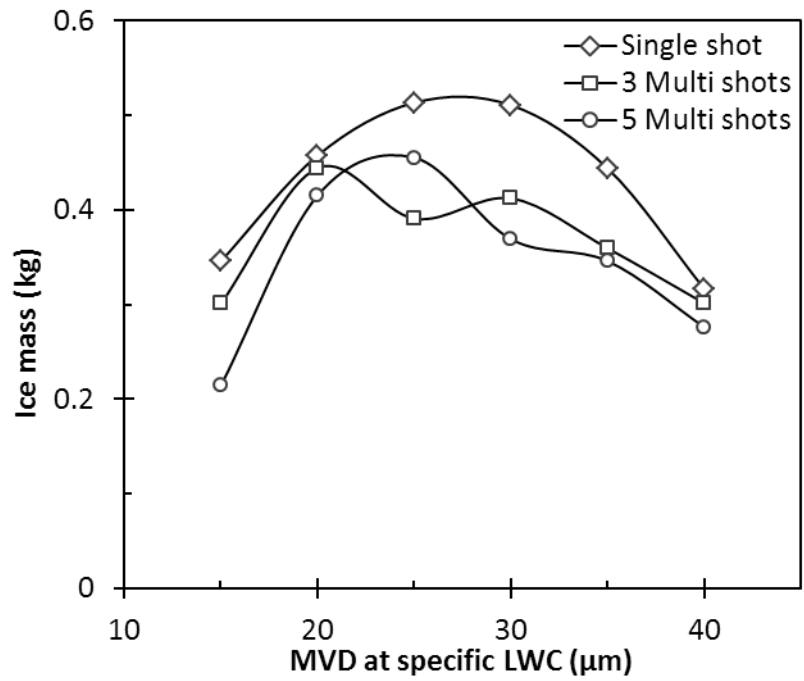


(a)

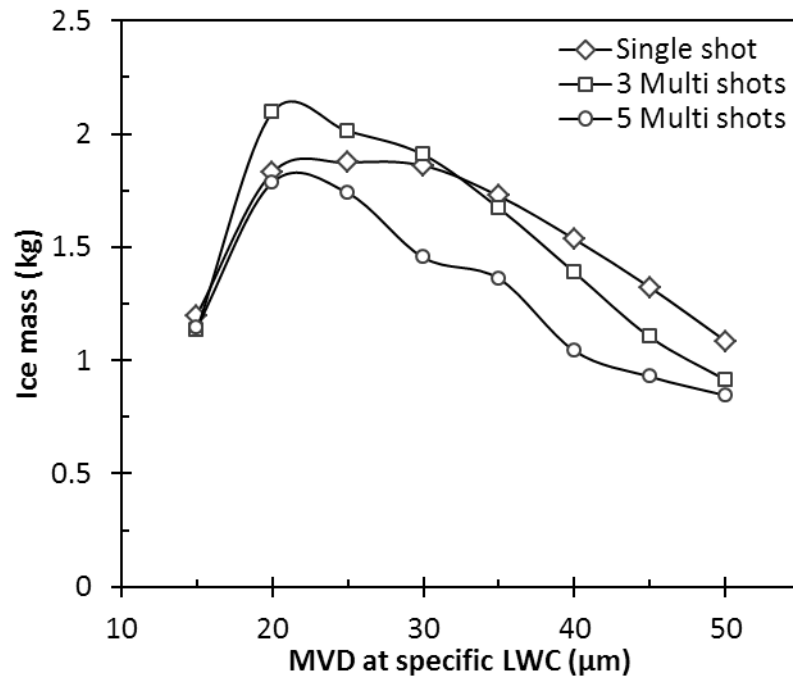


(b)

Figure (12) Ice mass variation with number of shots at -4°C in (a) low LWC conditions (stratiform clouds) and (b) high LWC conditions (cumuliform clouds)



(a)



(b)

Figure (13) Ice mass variation with number of shots at  $-4^{\circ}\text{C}$  with applied surface roughness in (a) low LWC conditions (stratiform clouds) and (b) high LWC conditions (cumuliform clouds)

#### 4.4. Ice Load Predications on NREL Airfoil Families

In this section, ice accumulation is investigated for NREL airfoil families. As presented in Table (1), one icing condition is maintained to investigate the effect of blade profile design / curvature on ice accumulation.

Table (1) Test conditions to examine curvature impact on ice mass

Parameter	Quantity
NREL airfoil families	From S801 to S835 (S824 data is not available)
Wind speed (m/s)	75
Icing temperature (°C)	-4
MVD value (μm)	30
LWC value (g/m <sup>3</sup> )	0.5
Blade thickness	100% (normal value corresponds to 1 m chord length)
Icing time (minutes)	30

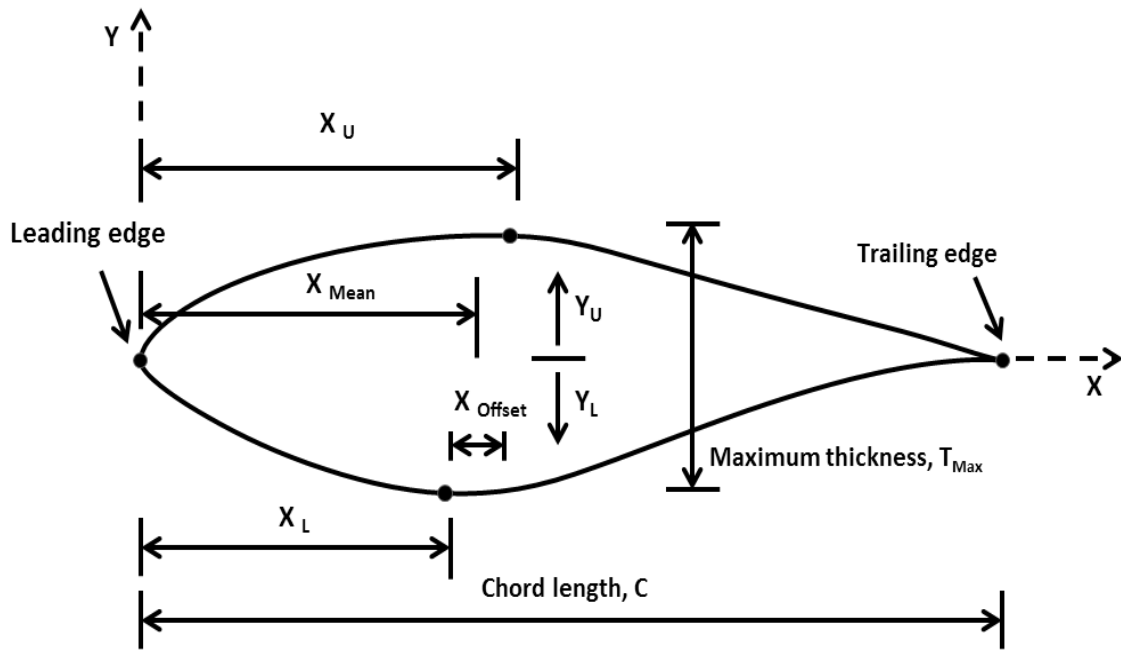
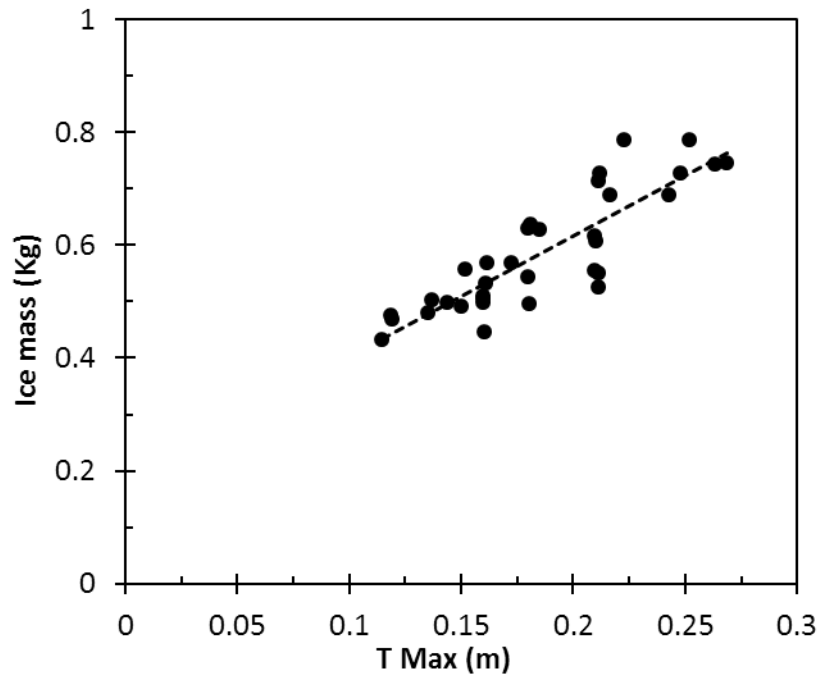


Figure (14) Airfoil curvature characterizations

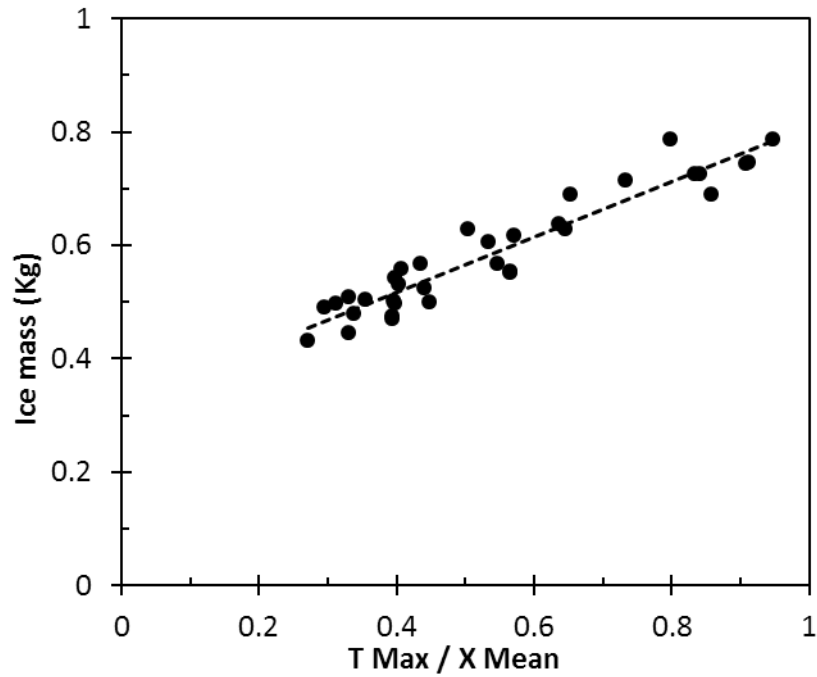
As illustrated in Fig. 14, airfoil curvature can be defined by  $X_U$ ,  $Y_U$ ,  $X_L$ ,  $Y_L$ ,  $X_{Offset}$ ,  $T_{Max}$ , and  $X_{Mean}$ . The variable  $X_{Offset}$  is the offset distance between the points  $(X_U, Y_U)$  and  $(X_L, Y_L)$ ,  $T_{Max}$  is blade maximum thickness and  $X_{Mean}$  is the average offset distance from

the origin ( $T_{Max}$  location on X axis). Blade curvature / leading edge radius is highly affected by the location of these two points ( $X_U, Y_U$ ) and ( $X_L, Y_L$ ) for both upper and lower sides, respectively.

As illustrated in Fig. 15, ice mass is significantly affected by both ice thickness and location. Locating  $X_{Offset}$  (distance between the two points ( $X_U, Y_U$ ) and ( $X_L, Y_L$ )) near the blade's leading edge can lead to a large stagnation area and increased ice accumulation. However, locating  $X_{Offset}$  near the blade's trailing edge can reduce the stagnation area and decrease the quantity of accumulated ice.



(a)



(b)

Figure (15) Ice mass variations with (a) blade maximum thickness and (b)  $T_{Max} / X_{Mean}$

As illustrated in Fig. 16, airfoils with more thickness tend to have greater ice accumulation compared to thinner airfoils. Thick blades have more stagnation area causing greater ice accumulation, however, differences between the upper and lower points on the X-axis ( $X_{Offset}$ ), can lead to various stagnation area configurations, which is the likely cause of airfoils with lower thickness having slightly equal or large ice quantity (i.e. comparing S802 with S803, S808 with S811 and S821 with S823).

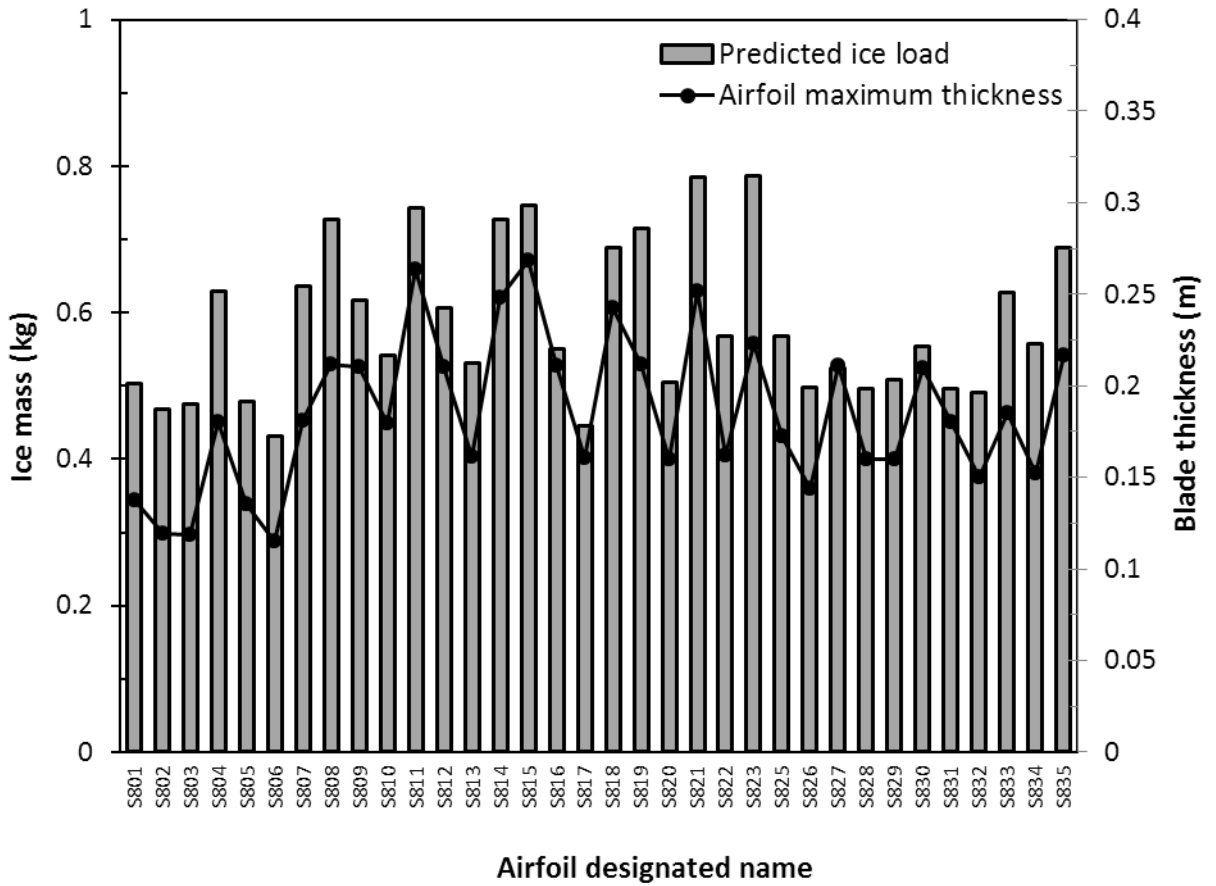


Figure (16) Ice loads on NREL airfoil families for HAWTs

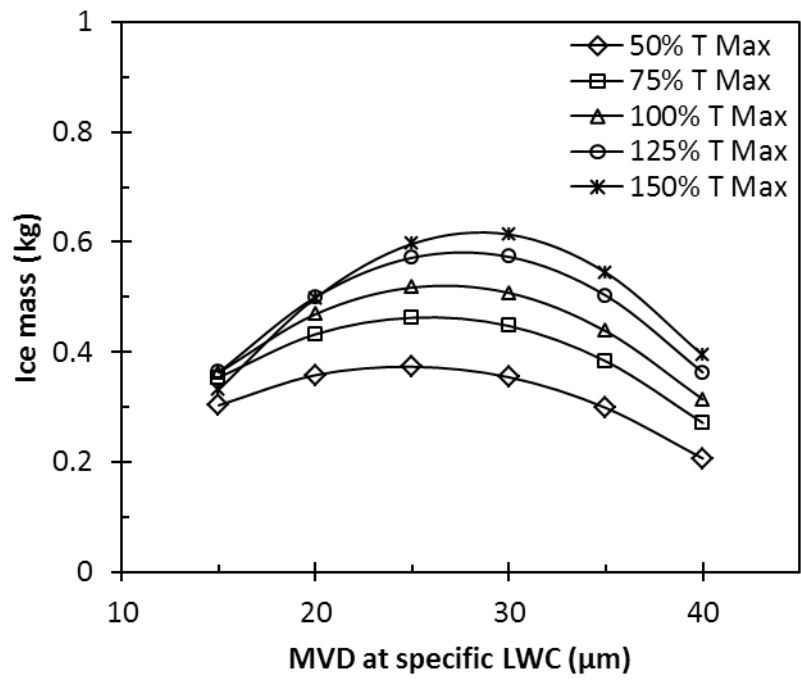
#### 4.5. Blade Thickness Effect

This section presents predicted ice accumulation on five different thicknesses of the same airfoil type, NREL S809, to investigate the relationship between blade thickness and icing conditions. As presented in Table (2), blade thickness is varied from 50% to 150% (where 100% value represents the original equivalent blade thickness for a chord length of 1 m), thus 50% thickness represents a thin blade and 150% thickness represents a thick blade.

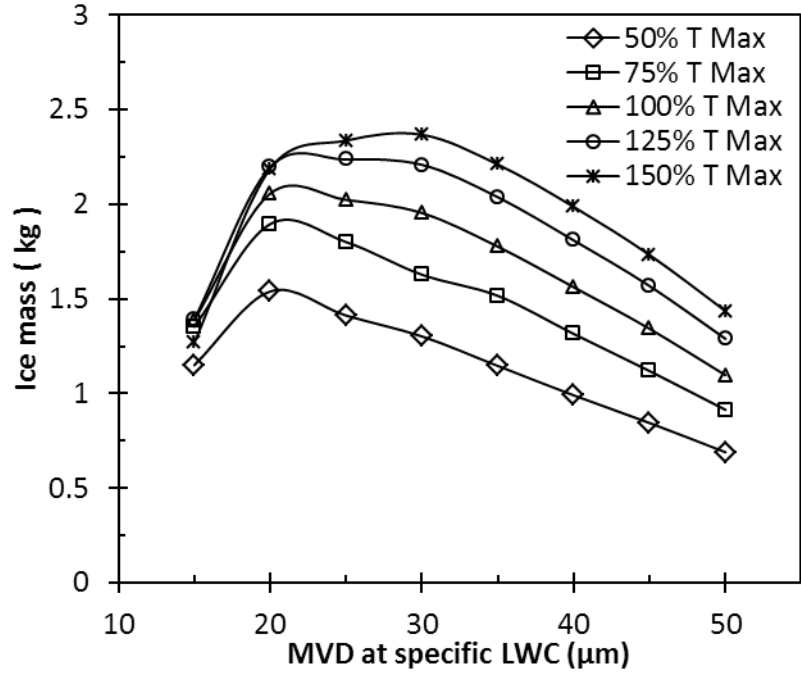
Table (2) Test conditions to examine blade thickness effect at various icing conditions

Parameter	Quantity				
Wind speed (m/s)	75				
Icing temperature (°C)	-4				
MVD value (µm)	Lower concentrations of LWC (g/m <sup>3</sup> )			Higher concentrations of LWC (g/m <sup>3</sup> )	
15	0.96			3.69564493	
20	0.740622842			3.25072738	
25	0.565769364			2.21371497	
30	0.422209486			1.62804482	
35	0.29344042			1.19854409	
40	0.174198124			0.892100294	
45	N/A			0.669194678	
50	N/A			0.488463681	
Blade thickness percentage of its normal value at 1 m chord length	50%	75%	100%	125%	150%
Blade thickness (m)	0.105011	0.157516	0.210021	0.262526	0.315032
Icing time (minutes)	30				

Flow field solutions are computed by FENSAP solver, and then droplet calculations for each icing conditions (LWC and MVD) are obtained using DROP 3D solver. Finally, icing calculations are predicted for each condition using a single shot approach. Icing conditions with low and high LWC conditions are investigated. Typically, smaller droplet sizes exist at higher LWC conditions while large droplets are at lower LWC conditions.



(a)



(b)

Figure (17) Ice mass variation with blade thickness for (a) low LWC conditions and (b) high LWC conditions

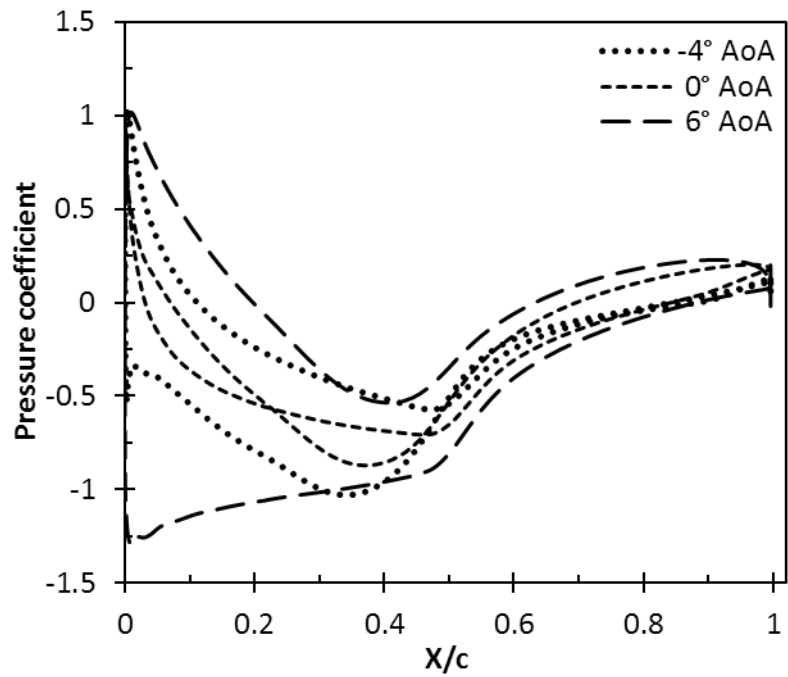
As illustrated in Fig. 17, for larger blade thicknesses higher quantities of ice are formed for differing icing conditions, which highlights the significance of blade thickness on ice load. For lower MVD, below 20  $\mu\text{m}$ , differences in ice mass do not change to the same extent as larger ones, highlighting the significance of MVD during ice accumulation. For larger droplet sizes, ice accretion variation with blade thickness is significant. Icing environments with small droplets at high LWC concentrations has a minor impact on ice amount compared to large droplets at lower LWC concentrations.

#### 4.6. Effect of Flow Angle of Attack on Ice Shape

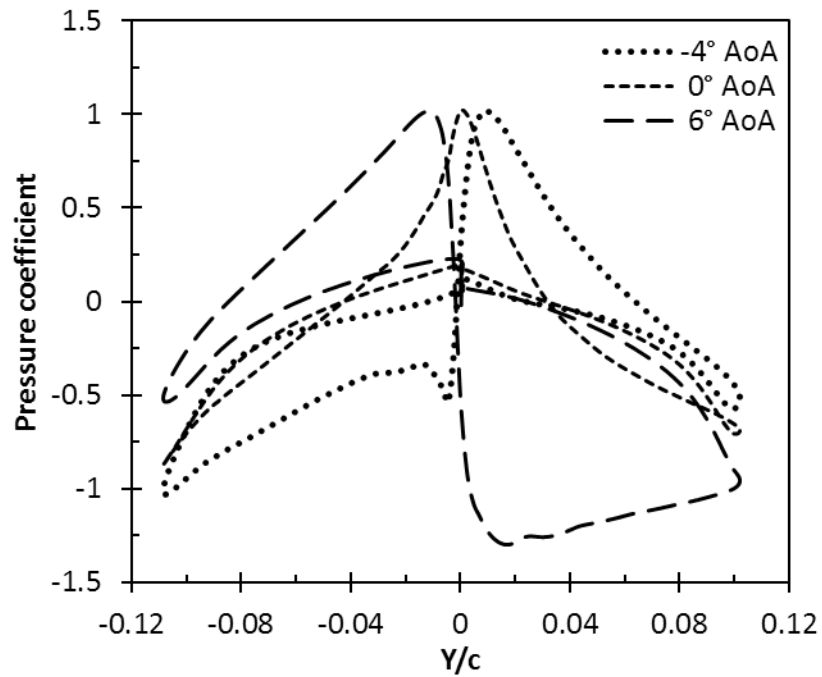
In this section, ice accretion on the wind turbine blade is investigated at different flow angles of attack. As presented in Table (3), numerically predicted ice shapes on NREL S809 using multi-shot approach are obtained at specific icing conditions.

Table (3) Test conditions to study flow angle of attack's effect on ice shape and mass

Parameter	Quantity
Wind speed (m/s)	75
Icing temperature ( $^{\circ}\text{C}$ )	-5
MVD value ( $\mu\text{m}$ )	30
LWC value ( $\text{g}/\text{m}^3$ )	0.3
Angle of attack ( $^{\circ}$ )	-4, -2, 0, 2, 4, 6
Icing time (minutes)	60



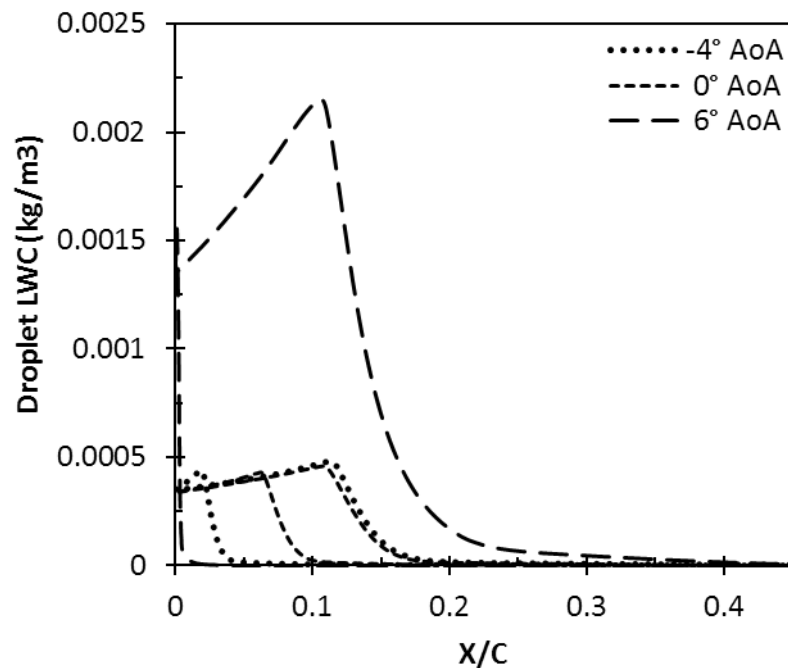
(a)



(b)

Figure (18) Power coefficient distribution variation for (a) chord length projection on the X-axis and (b) blade height projection on the Y-axis

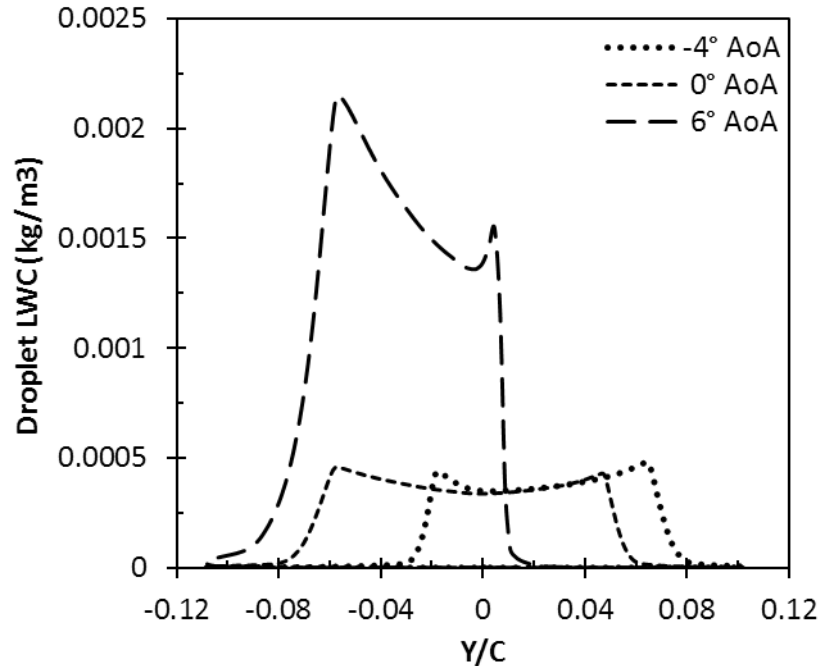
As illustrated in Fig. 18, each curve represents the pressure distribution on two sides of the blade where blade pressure side is represented by positive values of  $y/c$  and blade suction side is represented by negative values of  $y/c$ , pressure coefficient on a blade surface varies with flow angle since the location of stagnation point changes. As illustrated in Fig. 18a, maximum values can be found at the blade leading edge due to flow stagnation with blade edge. As illustrated in Fig. 18b, the behaviour of both pressure and suction sides are not identical at zero flow angle of attack due to the asymmetry of the airfoil curvature.



(a)

As shown in Fig. 19, as multiphase flow (air and water droplets) collides with a blade surface at different AoA, the LWC concentrations around blade surface vary. As

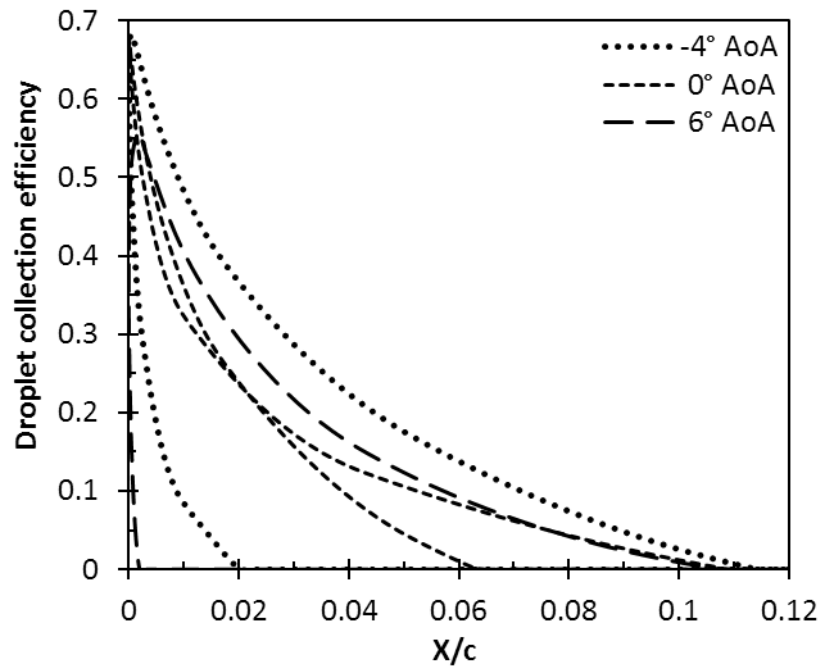
illustrated in Fig. 19a, high values can exist at the blade's leading edge which is likely the cause of the majority of ice accretion at the blade's edge.



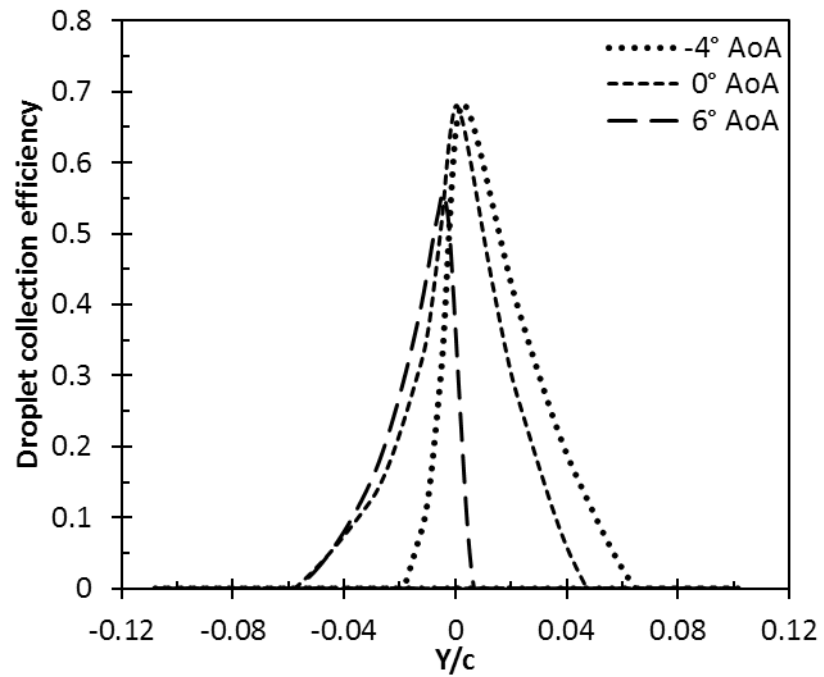
(b)

Figure (19) Droplet LWC concentrations variation for (a) chord length projection on the X-axis and (b) blade height projection on Y axis

As flow separates no droplet LWC concentrations are present in the last 60% portion of blade section. As illustrated in Fig. 19b, higher LWC concentrations are expected at higher flow angles of attack. Changing of stagnation point can change the LWC distribution range on Y axis. Comparatively low LWC concentrations can be at the stagnation point which illustrates the reason that ice thickness is minimal at this point.



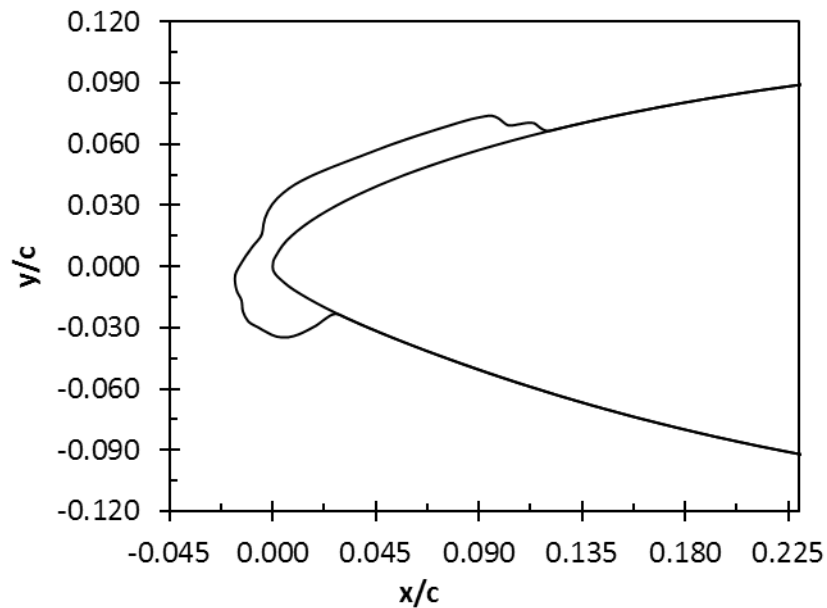
(a)



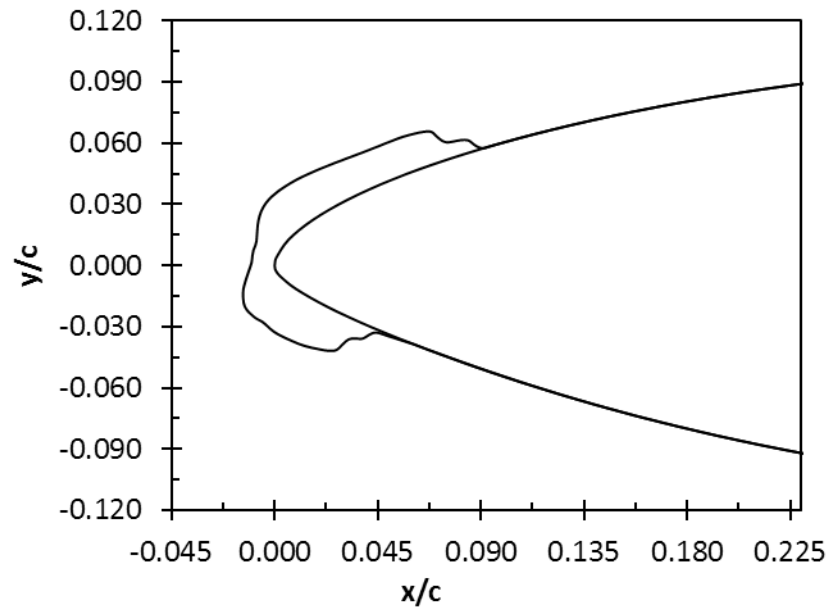
(b)

Figure (20) Droplet collection efficiency variation for (a) chord length projection on X-axis and (b) blade height projection on Y-axis

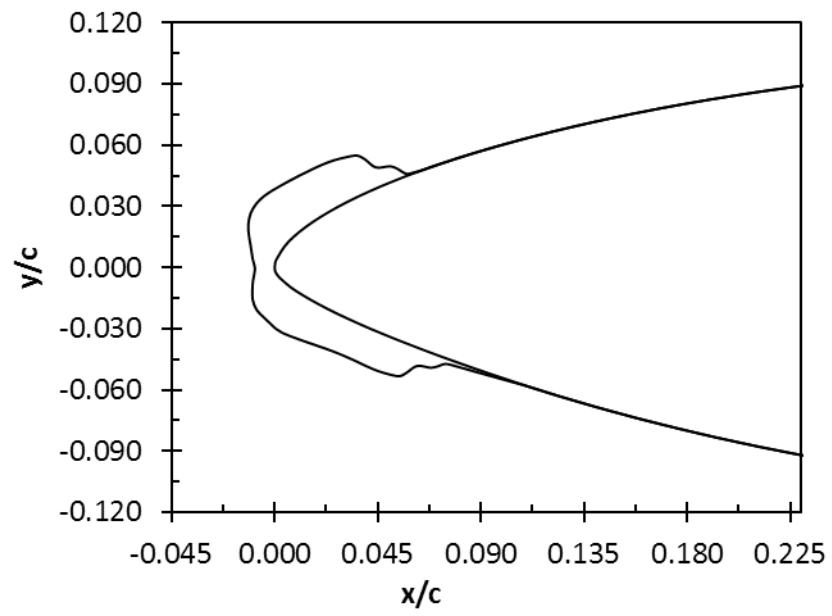
Collection efficiency is a parameter that describes the effective collision forces of droplets on a blade surface, and is dimensionless parameter. Fig. 20 illustrates droplet collection efficiency variation along blade chord location on X axis and blade thickness projection on Y axis at different AoA. Its peak value is mainly found at the stagnation point and its location on Y axis varies significantly with angle of attack, as in the case of 6°. As illustrated in Fig. 21, ice accretion is mainly found at the leading edge of a wind turbine blade. However, its location on the leading edge depends on the flow angle during ice accumulation. Negative flow angles accumulate ice on the pressure side and positive angles generate ice on the suction side of the blade. This is likely due to the changing location in flow stagnation point with the flow's angle of attack. Thus, if the stagnation point is located on pressure side more ice quantity will be formed on this side compared to suction side.



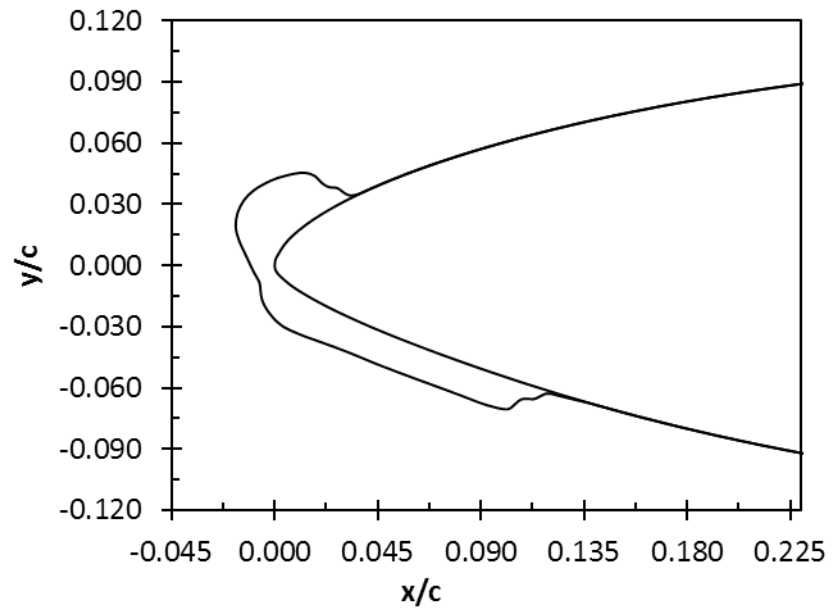
(a)



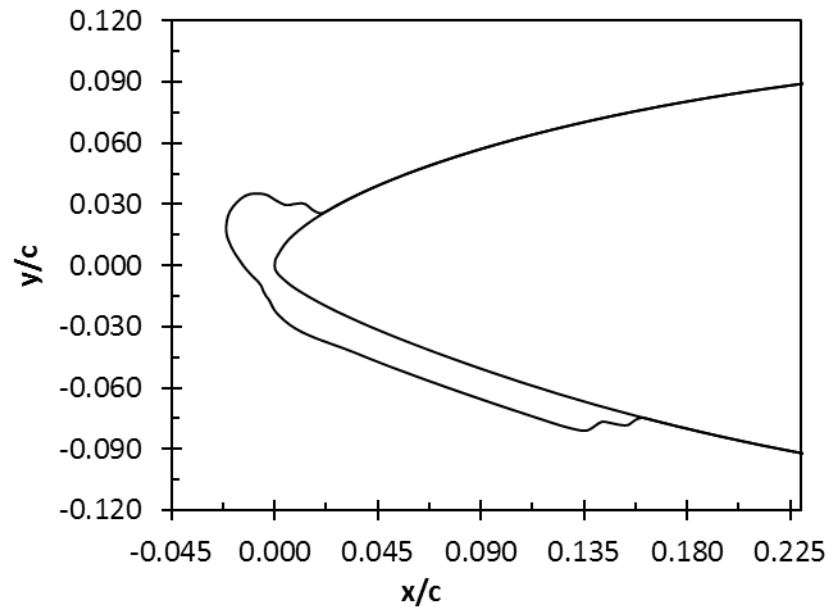
(b)



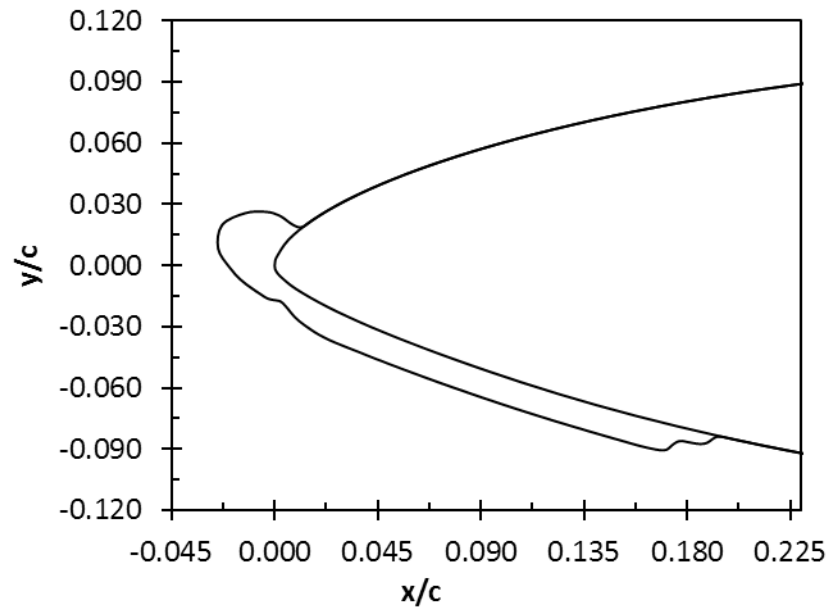
(c)



(d)



(e)



(f)

Figure (21) Ice shapes at different flow angles of attack: (a)  $-4^\circ$ , (b)  $-2^\circ$ , (c)  $0^\circ$ , (d)  $2^\circ$  (e)  $4^\circ$  and (f)  $6^\circ$

Furthermore, the droplet collection and impingement profiles are affected by the flow's angle of attack. At zero angle of attack, ice quantity on the pressure and suction blade sides differs due to the airfoil's asymmetry. Lower ice thickness can be found at the flow stagnation point located on leading edge curve. Ice propagation on blade sides can increase with the increase of flow attacking angle. However, for the same icing condition, total ice quantity is relatively consistent for the different flow angles examined.

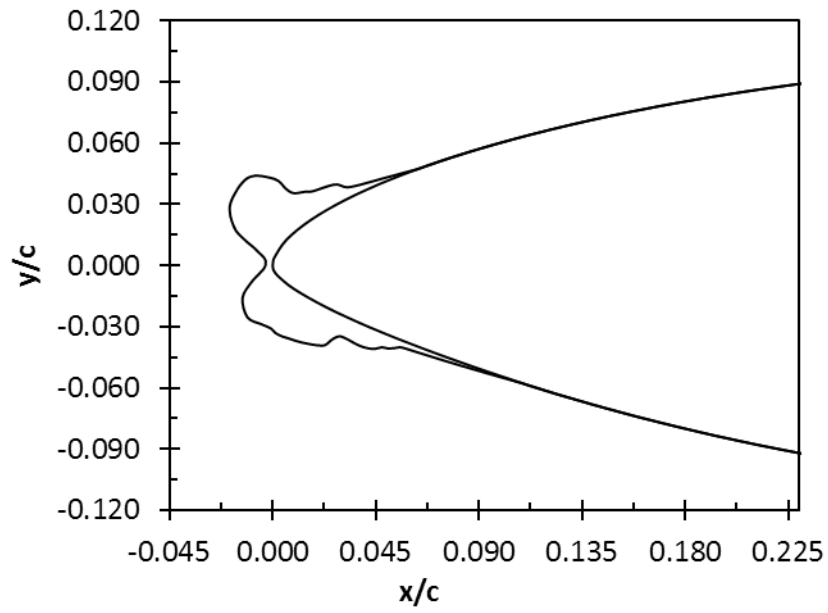
#### 4.7. Icing Effect on Aerodynamic Performance

Aerodynamic characteristics significantly depend on blade curvature. During an ice accretion process, the blade profile changes with time, changing both lift and drag characteristic. As shown in Table (4), different icing conditions are examined to numerically obtain various ice shapes. This comparison between clean and iced profiles can be used to estimate the changes in aerodynamic performance.

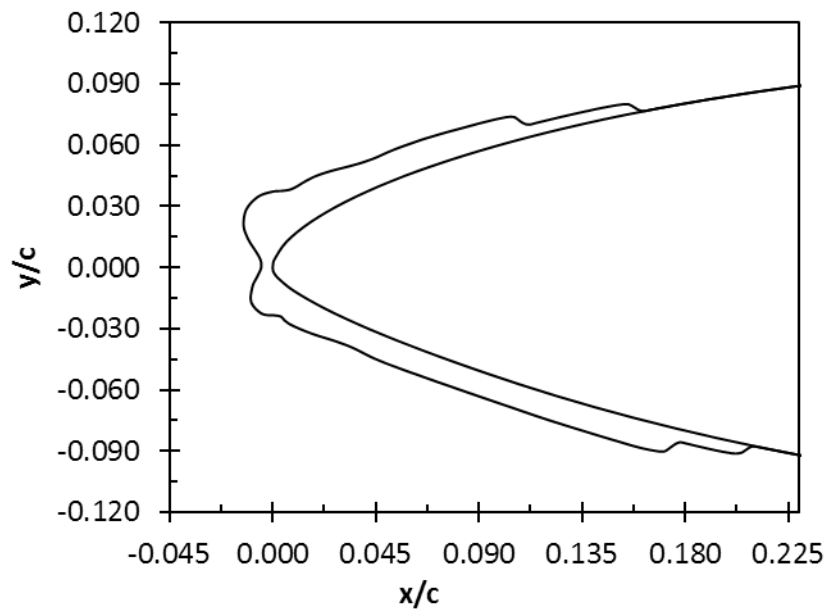
Table (4) Test conditions to examine blade aerodynamics during icing conditions

Parameter	Quantity
Airfoil designated name	NREL S809
AoA (°)	0
Wind speed (m/s)	75
Icing temperature (°C)	-4, -8
MVD value (µm)	30
LWC value (g/m <sup>3</sup> )	0.5, 1
Blade thickness	0.210021 m (Normal maximum thickness corresponds to a chord length of 1 m)
Icing time (minutes)	30

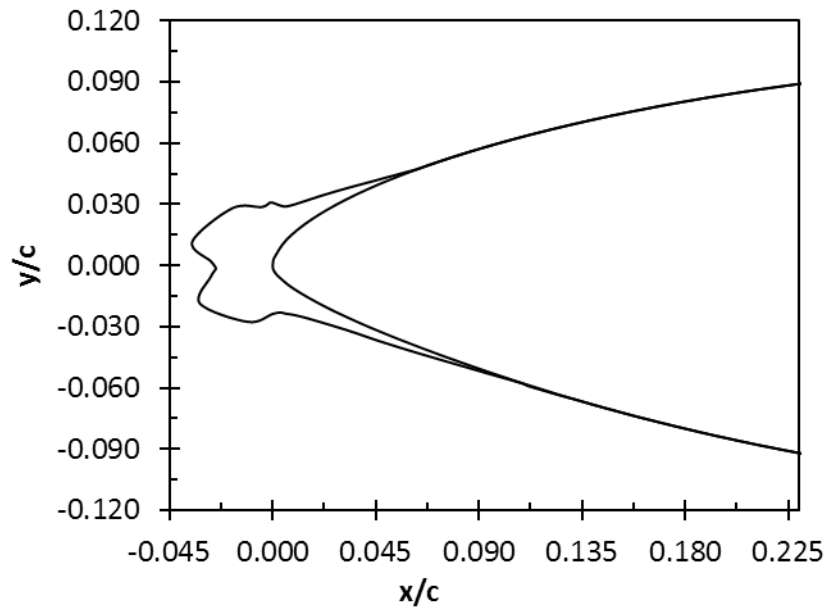
As ice accretes on the blade surface, aerodynamics change and considerably affect flow field, heat fluxes and droplet impingement dynamics. Multi-shot approach in FENSAP ICE solver accounts for the transient changes occurring during an ice formation process. Thus, multi-shot approach is used to accurately predict ice shapes for this analysis.



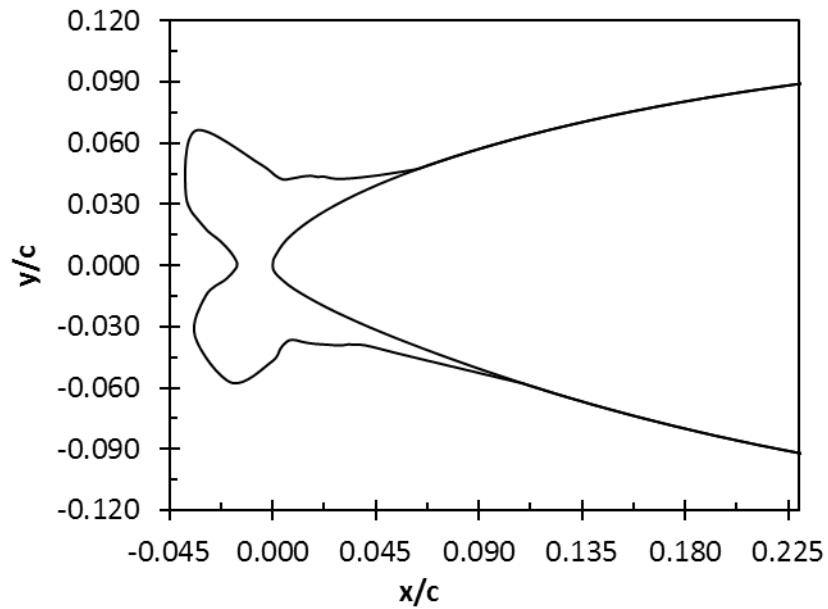
(a)



(b)



(c)

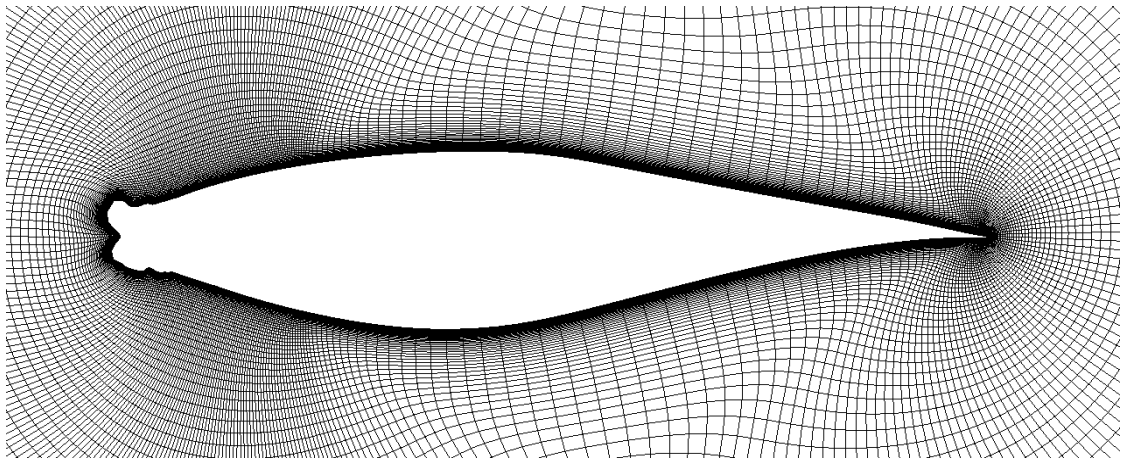


(d)

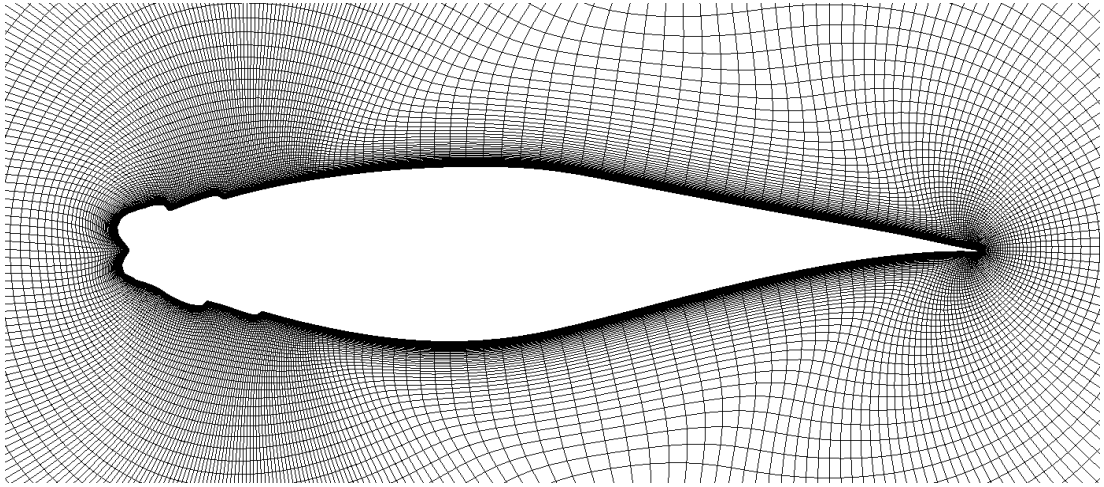
Figure (22) Numerically predicted ice shapes for different icing conditions at (a) LWC = 0.5 g/m<sup>3</sup>, T = -4°C, (b) LWC = 1 g/m<sup>3</sup>, T = -4°C, (c) LWC = 0.5 g/m<sup>3</sup>, T = -8°C and (d) LWC = 1 g/m<sup>3</sup>, T = -8°C

As illustrated in Fig. 22, ice shapes at  $-4^{\circ}\text{C}$  and  $-8^{\circ}\text{C}$  temperatures with two LWC conditions are numerically predicted using a multi-shot approach. Generally, icing shape and location are controlled by flow speed and angle of attack. Ice thickness at the stagnation point of the flow is highly influenced by the atmospheric temperature, as ice thickness at this point is increased when comparing ice shapes at  $-4^{\circ}\text{C}$  and  $-8^{\circ}\text{C}$ , under fixed LWC and MVD conditions.

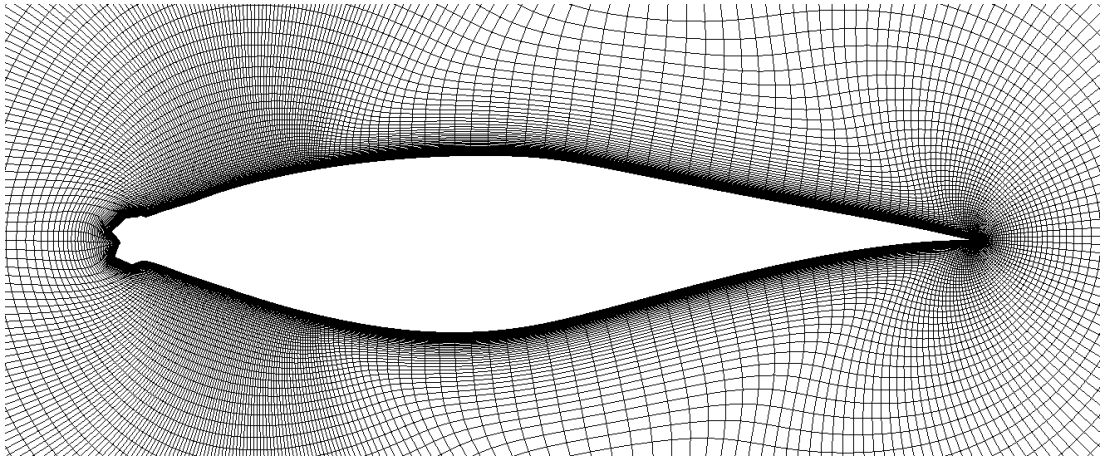
At  $-4^{\circ}\text{C}$ , LWC significantly affects the quantity of ice accumulation, as well as its propagation along the blade section. At  $-8^{\circ}\text{C}$ , a horn ice shape is formed and its thickness / height are affected by LWC. As illustrated in Fig. 23, a computational grid around an iced NREL S809 blade is created for each ice shape to numerically predict the lift and drag coefficients.



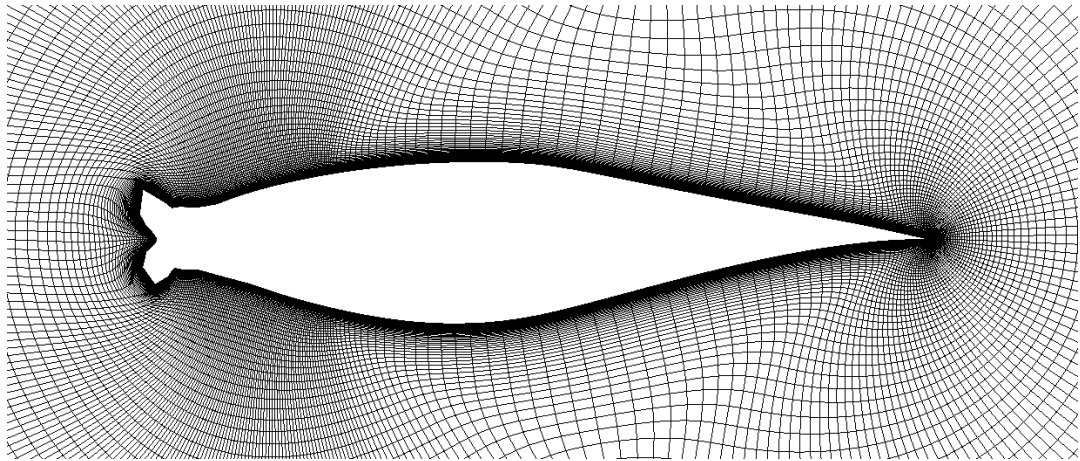
(a)



(b)



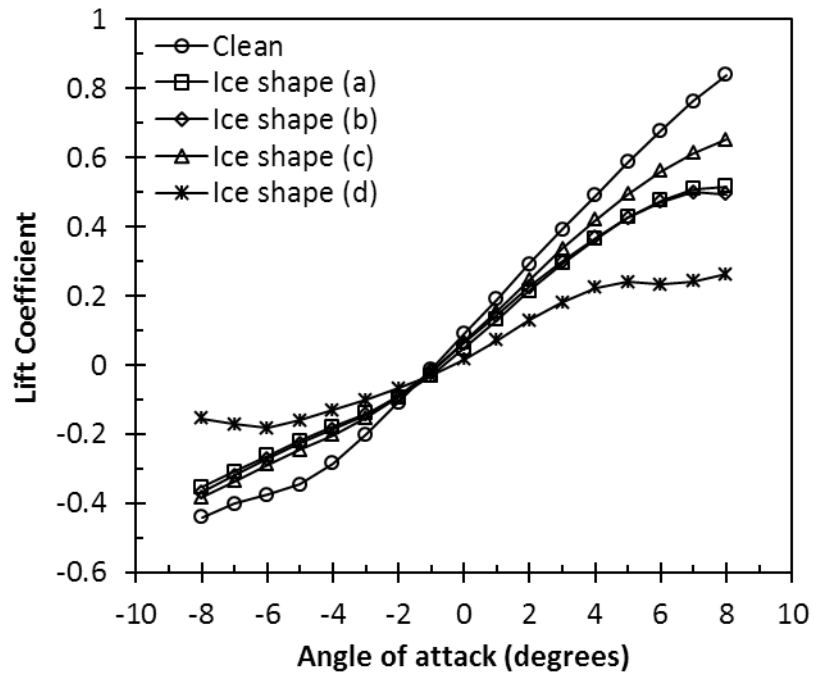
(c)



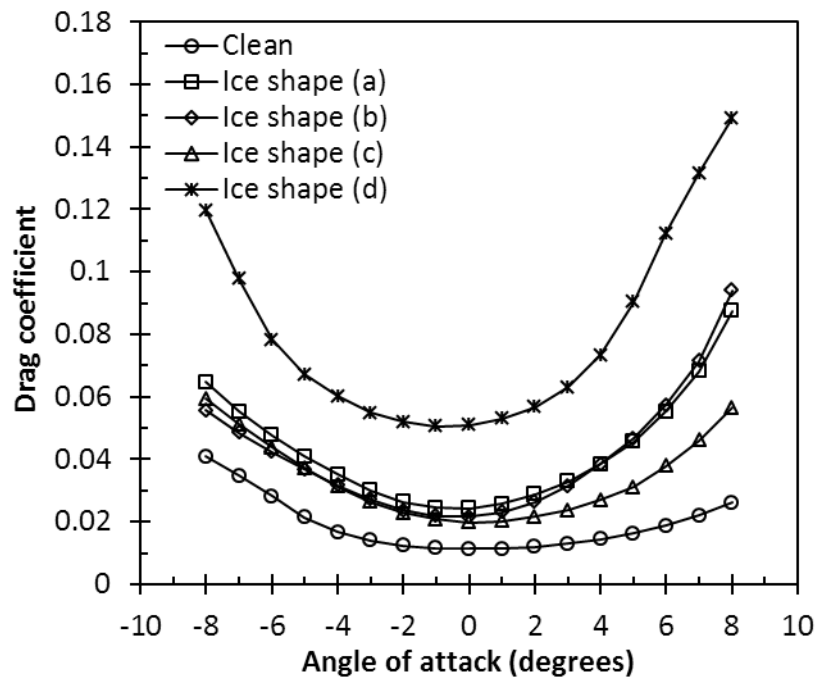
(d)

Figure (23) Computational grids around airfoils with accreted ice for different icing conditions: (a)  $LWC = 0.5 \text{ g/m}^3$ ,  $T = -4^\circ\text{C}$ , (b)  $LWC = 1 \text{ g/m}^3$ ,  $T = -4^\circ\text{C}$ , (c)  $LWC = 0.5 \text{ g/m}^3$ ,  $T = -8^\circ\text{C}$  and (d)  $LWC = 1 \text{ g/m}^3$ ,  $T = -8^\circ\text{C}$

The Reynolds number is maintained at  $5.8 \times 10^6$  m. As illustrated in Fig. 24, ice accretion can produce degradation of the lift coefficient, as well as increase drag due to induced roughness. Every ice distribution can cause different flow characteristics around the blade, including location of flow stagnation point (affected by angle of attack) and flow separation behaviour (affected by height / thickness of the ice horn). As illustrated in Fig. 24, aerodynamic behaviour is not identical when comparing positive angles with negative angles due to the asymmetry in airfoil curvature. A significant drop in lift coefficient ranging from 10% to 65% is predicted by the simulations. Furthermore, the increase in drag and decrease in lift is substantial for large horn ice. As wind turbine blade lift decreases the overall torque will decrease leading to a reduction in output power.



(a)



(b)

Figure (24) Aerodynamic performance for predicted ice shapes, in terms of (a) lift coefficient and (b) drag coefficient

#### 4.8. Results Validation

A study [47] on icing of NACA 0012 airfoils using LEWICE code and wind tunnel tests is used to validate this work in terms of ice shape. A computational grid is created around NACA 0012 with the same process and configurations used for NERL S809. As presented in Table (5), one condition from the experiment [31] is investigated using FENSAP ICE solver, to obtain an ice shape comparison.

Table (5) Test conditions for validation of numerical predictions

Parameter	Quantity
Chord length	0.53 m
Air speed	67.1 m/s
LWC	1.0 g/m <sup>3</sup>
MVD	20 μm
AoA	4°
Temperature	-7.78°C
Icing time	6 min

As illustrated in Fig. 25 and 26, the predicted ice shapes by FENSAP ICE agree well with both numerical and experimental data. For 5 ice shots, the ice horn thickness (0.025) at the leading edge is nearly equal to the one predicted by experimental investigation [47]. Changes in ice shapes can be formed depending on number of ice shots. Therefore, based on nearly equal ice shapes when comparing FENSAP ICE data with experimental data, ice mass is nearly identical.

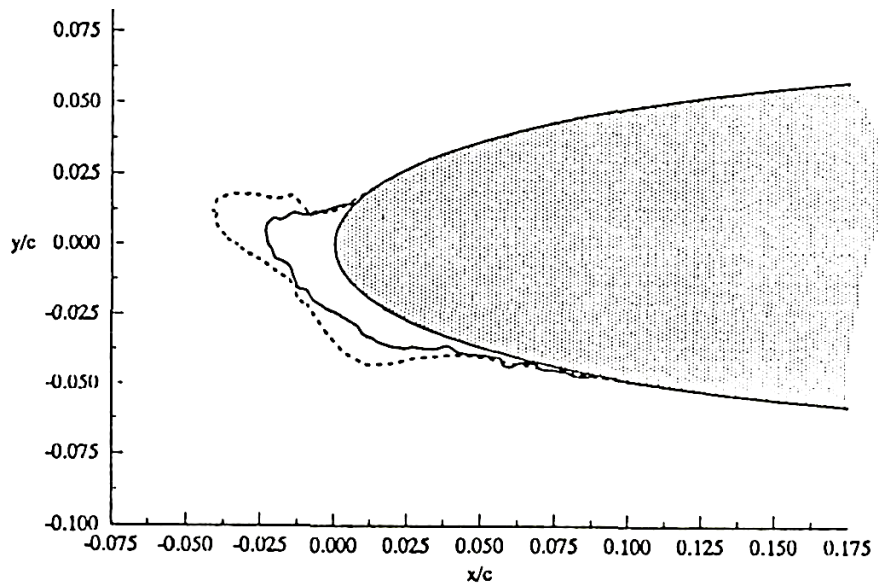


Figure (25) Ice accretion on NACA 0012 obtained numerically using LEWICE (dashed line) and experimentally (solid line) [47]

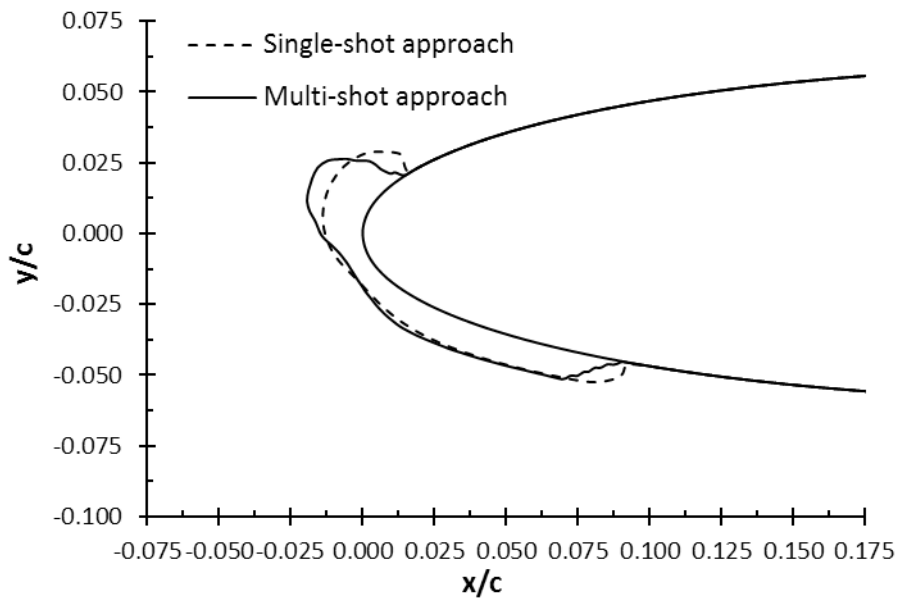


Figure (26) Accretion shapes on NACA 0012 modeled by FENSAP ICE for comparison

For aerodynamic efficiency prediction due to ice accumulation, the experimental results analysed by Broeren and Bragg [48, 49] at Reynolds number equals  $6.5 \times 10^{-6}$  m showed that the drop in the aerodynamic efficiency can range from 15% to 80% due to ice accretion. The current predicted results in this research regarding the aerodynamic loss due to ice agree well with the experimental results analysed by Broeren and Bragg [48, 49], since drag is increased significantly and a reduction in lift coefficient ranging from 10% to 65% is resulted.

## Chapter 5 Conclusions and Recommend Research

In this thesis, ice accretion on a wind turbine blade section for stratiform and cumuliform environments was numerically investigated using FENSAP ICE solver. Maximum ice loads can be expected at  $-4^{\circ}\text{C}$ ; hence glaze ice accretion is more severe for wind turbines in terms of its mass. Power used for anti-icing and de-icing systems would be higher during warmer temperatures ranges ( $-3^{\circ}\text{C}$  to  $-8^{\circ}\text{C}$ ). Consequently more power loss percentage can be predicted for cumuliform cloud conditions. As LWC decreases with altitude, ice accretion load is expected to decrease with elevation. Therefore, for cold and harsh environments, it is better for wind turbines to be located at higher elevations. Blade surface roughness can significantly affect ice accretion in terms of mass and shape, especially at temperatures (around  $-2^{\circ}\text{C}$ ) with higher LWC conditions.

Ice load predictions on NREL airfoil families was investigated, showing that ice mass is highly influenced by both blade thickness and location. Thus, thicker blade sections near the tip should be avoided as it can lead to large ice loads under different icing conditions. The predicted results showed that droplet size has a significant effect on ice accumulation for fixed temperature and LWC conditions. Higher angles of attack can significantly impact ice accretion physics. Ice accretion on wind turbine blade can significantly increase drag coefficient. The loss in lift coefficient was estimated to range from 10% to 65% for a blade section. Integrating the loss percentage along the blade span shows the degradation of blade performance. Thus, ice accretion can significantly reduce power production.

The results of this thesis provide useful new insights into ice accretion rates on wind turbine blades for numerous conditions, as well as valuable new numerical data to better enable wind turbines for remote communities located in cold / harsh environments.

### **Recommended research**

Future work could include full twisted blade models that can be used to investigate different ice accretion variables, as well as detailed optimization study of the blade geometric parameters to minimize the ice accretion effects. Future work could also include an investigation of icing on whole blade performance and prediction of overall power loss due to ice, as well as icing wind tunnel verification of these results.

A major area of concern for optimizing wind turbine operation during an icing event is investigation of power loss as a function of time. There is not adequate research available on this subject for wind turbines, but an undeniable opportunity to improve operation schemes for iced wind turbines exists. Measuring performance data for iced airfoils over a time interval could also be used to validate simulations of wind turbine icing. An important field is to measure the climate conditions (i.e. wind speed, LWC, MVD, and temperature variations) at wind turbine site during icing events, then using this data to investigate ice numerically and experimentally. So that power loss for de-icing techniques and mitigation strategies can be predicted. Investigation of de-icing techniques should be investigated experimentally on a small blade portion.

## References

- [1] Kreith, F. and Krumbieck, S. (2013) Principles of sustainable energy systems, CRC press.
- [2] Battisti, L. (2015) Wind turbines in cold climates: Icing impacts and mitigation systems. Springer.
- [3] Hudecz, A., Koss, H. and Hansen, M., Ice accretion on wind turbine blades, 15th International Workshop on Atmospheric Icing of Structures (IWAIS XV), January, 2013.
- [4] Canwea (2017) Canada wind energy installed capacity, Retrieved from <http://canwea.ca/wind-energy/installed-capacity/>.
- [5] Jasinski, W., Noe, S., Selig, M. and Bragg, M. (1997) Wind turbine performance under icing conditions. 35th Aerospace Sciences Meeting and Exhibit.
- [6] Tammelin, B., Holttinen, H., Morgan, C., Richert, F., Seifert, H., Säntti, K. and Vølund (2000) Wind energy production in cold climate.
- [7] Cattin, R. (2013) Icing of wind turbines, Vindforsk projects, A survey of the development and research needs, Elforsk report 13.
- [8] Hochart, C., Fortin, G., Perron, J. and Ilinca, A. (2008) Wind turbine performance under icing conditions, Wind Energy 11(4): 319-333.

- [9] Botta, G., Cavaliere, M. and Holttinen, H. (1998) Ice accretion at acqua spruzza and its effects on wind turbine operation and loss of energy production, Hetta, Finland, 77-86.
- [10] Homola, M. (2005) Impacts and causes of icing on wind turbines. Navrik University College Report.
- [11] Battisti, L. (2015) Relevance of icing for wind turbines, Wind Turbines in Cold Climates Springer International Publishing, 43-111.
- [12] Parent, O. and Ilinca, A. (2011) Anti-icing and de-icing techniques for wind turbines: Critical review, Cold regions science and technology, 65(1): 88-96.
- [13] Virk, M. S., Homola, M. C. and Nicklasson, P. J. (2012) Atmospheric icing on large wind turbine blades, International Journal of Energy and Environment, 3(1): 1-8.
- [14] Makkonen, L. (2000) Models for the growth of rime, glaze, icicles and wet snow on structures, Philosophical Transactions of the Royal Society of London A: Mathematical, Physical and Engineering Sciences, 358(1776): 2913-2939.
- [15] Fikke, S. M., Ronsten, G., Heimo, A., Kunz, S., Ostrozlik, M., Persson, P. E. and Laakso, T. (2006) Atmospheric icing on structures: measurements and data collection on icing: state of the art, Meteo Schweiz.
- [16] Jeck, R. K. (2002). Icing Design Envelopes (14 CFR Parts 25 and 29, Appendix C) Converted to a Distance Based Format (No. DOT/FAA/AR-00/30). FEDERAL AVIATION ADMINISTRATION TECHNICAL CENTER ATLANTIC CITY NJ.

- [17] Cober, S. G., Isaac, G. A. and Strapp, J. W. (2001) Characterizations of aircraft icing environments that include supercooled large drops. *Journal of Applied Meteorology*, 40(11): 1984-2002.
- [18] Masters, C. O. (1985) A new characterization of super cooled clouds below 10,000 feet AGL.
- [19] Fortin, G. and Perron, J. Wind turbine icing and de-icing. 47th AIAA Aerospace Sciences Meeting including The New Horizons Forum and Aerospace Exposition, 2009.
- [20] Homola, M. C., Nicklasson, P. J. and Sundsbø, P. A. (2006) Ice sensors for wind turbines. *Cold regions science and technology*, 46(2): 125-131.
- [21] Addy, H., Sheldon, D., Potatpczuk, Jr, M., Addy, H., Sheldon, D. and Potatpczuk, Jr, M. Modern airfoil ice accretions. 35th Aerospace Sciences Meeting and Exhibit, march 1997.
- [22] Shin, J. and Bond, T. (1992, January) Results of an icing test on a NACA 0012 airfoil in the NASA Lewis Icing Research Tunnel. 30th Aerospace Sciences Meeting and Exhibit.
- [23] Bowden, D. T., Gensemer, A. E. and Skeen, C. A. (1963) Engineering summary of airframe icing technical data. GENERAL DYNAMICS SAN DIEGO CA CONVAIR DIV.
- [24] Tsuboi, K., & Kimura, S. Numerical simulation of ice accretion on a body with droplet flow Model. 14th Computational Fluid Dynamics Conference, 1999.

- [25] Snellen, M., Boelens, O., Hoeijmakers, H. W. M. A., Snellen, M., Boelens, O. and Hoeijmakers, H. A computational method for numerically simulating ice accretion. 15th Applied Aerodynamics Conference, 1997.
- [26] Ruff, G. A. and Berkowitz, B. M. (1990) User's manual for the NASA Lewis ice accretion prediction code (LEWICE).
- [27] Marjaniemi, M., Makkonen, L. and Laakso, T. (2000) TURBICE-the wind turbine blade icing model. In Proceedings of the BOREAS V conference.
- [28] Makkonen, L., Laakso, T., Marjaniemi, M. and Finstad, K. (2001) Modelling and prevention of ice accretion on wind turbines. *Wind Engineering*, 25(1): 3-21.
- [29] Ayabakan, S. (1991) The Turbine Blade Icing Model (TURBICE) and its further development via a new interface.
- [30] Hé, lo-iacute, Beaugendre, S., Fran-tilde, Morency, O. and Habashi, W. G. (2003) FENSAP-ICE's three-dimensional in-flight ice accretion module. ICE3D. *Journal of Aircraft*, 40(2): 239-247.
- [31] Habashi, W. G., Morency, F. and Beaugendre, H. FENSAP-ICE: A Comprehensive 3D Simulation Tool for In-flight Icing. 7th International Congress of Fluid Dynamics and Propulsion, Sharm-El-Sheikh, Egypt, December 2001.
- [32] Beaugendre, H., Morency, F. and Habashi, W. ICE3D, FENSAP-ICE'S 3D in-flight ice accretion module. 40th AIAA Aerospace Sciences Meeting and Exhibit, January, 2002.

- [33] Homola, M. C., Wallenius, T., Makkonen, L., Nicklasson, P. J. and Sundsbø, P. A. (2010) Turbine size and temperature dependence of icing on wind turbine blades. *Wind Engineering*, 34(6): 615-627.
- [34] Fu, P. and Farzaneh, M. (2010) A CFD approach for modeling the rime ice accretion process on a horizontal axis wind turbine. *Journal of Wind Engineering and Industrial Aerodynamics*, 98(4): 181-188.
- [35] Bose, N. (1992) Icing on a small horizontal-axis wind turbine - Part 1: Glaze ice profiles. *Journal of wind engineering and industrial aerodynamics*, 45(1): 75-85.
- [36] Bose, N. (1992) Icing on a small horizontal-axis wind turbine - Part 2: Three dimensional ice and wet snow formations. *Journal of Wind Engineering and Industrial Aerodynamics*, 45(1): 87-96.
- [37] Virk, M. S., Homola, M. C. and Nicklasson, P. J. (2010) Effect of rime ice accretion on aerodynamic characteristics of wind turbine blade profiles. *Wind Engineering*, 34(2): 207-218.
- [38] Hudecz, A., Koss, H. and Hansen, M. O. L. Ice accretion on wind turbine blades. 15th International Workshop on Atmospheric Icing of Structures (IWAIS XV), 2013.
- [39] Barber, S., Wang, Y., Jafari, S., Chokani, N. and Abhari, R. S. (2011) The impact of ice formation on wind turbine performance and aerodynamics. *Journal of Solar Energy Engineering*, 133(1): 011007.

- [40] Homola, M. C., Virk, M. S., Wallenius, T., Nicklasson, P. J. and Sundsbø, P. A. (2010) Effect of atmospheric temperature and droplet size variation on ice accretion of wind turbine blades. *Journal of wind engineering and industrial aerodynamics*, 98(12): 724-729.
- [41] Lamraoui, F., Fortin, G., Benoit, R., Perron, J. and Masson, C. (2014) Atmospheric icing impact on wind turbine production. *Cold Regions Science and Technology*, 100: 36-49.
- [42] Reid, T., Baruzzi, G., Ozcer, I., Switchenko, D., and Habashi, W. FENSAP-ICE simulation of icing on wind turbine blades, part 1: performance degradation. 51st AIAA aerospace sciences meeting including the new horizons forum and aerospace exposition, Grapevine, Texas, January, 2013.
- [43] Tangier, J. L. and Somers, D. M. (1995) NREL airfoil families for HAWTs National Renewable Energy Laboratory, 117-123.
- [44] Cao, Y., Ma, C., Zhang, Q. and Sheridan, J. (2012) Numerical simulation of ice accretions on an aircraft wing. *Aerospace Science and Technology*, 23(1): 296-304.
- [45] ANSYS (2015) FENSAP-ICE user manual R1.0, Canada.
- [46] Spalart, P. and Allmaras, S. A one-equation turbulence model for aerodynamic flows. 30th aerospace sciences meeting and exhibit, January, 1992.

[47] Shin, J. and Bond, T. H. (1992) Experimental and computational ice shapes and resulting drag increase for a NACA 0012 airfoil.

[48] Broeren, A. P., Bragg, M. B. and Addy, H. E. (2004) Effect of intercycle ice accretions on airfoil performance. *Journal of Aircraft*, 41(1): 165-174.

[49] Horák, V., Rozehnal, D., Chára, Z. and Hyll, A. (2008) CFD AND EXPERIMENTAL STUDY OF AERODYNAMIC DEGRADATION OF ICED AIRFOILS.